International Journal of Biological Macromolecules 339 (2026) 149845

Contents lists available at ScienceDirect

International Journal of Biological Macromolecules

journal homepage: www.elsevier.com/locate/ijbiomac

Spatiotemporally activated gelatin/unzipped carbon nanotubes/chitosan-based conductive hydrogel via dual stimuli for robust methicillin-resistant *Staphylococcus aureus* biofilm eradication

Tejal V. Patil [a,b,c], Aayushi Randhawa [a,b], Hyeonseo Park [a,b], Rumi Acharya [a,b], Sayan Deb Dutta [a,c], Ki-Taek Lim [a,b,c,*]

[a] Department of Biosystems Engineering, Kangwon National University, Chuncheon, 24341, Republic of Korea
[b] Interdisciplinary Program in Smart Agriculture, Kangwon National University, Chuncheon, 24341, Republic of Korea
[c] Institute of Forest Science, Kangwon National University, Chuncheon, 24341, Republic of Korea

ARTICLE INFO

Keywords:
Conductive chitosan
Antibacterial hydrogel
Biofilm
NIR
Electrical stimulation
Mechanism

ABSTRACT

Antibiotic-resistant bacteria, especially methicillin-resistant *Staphylococcus aureus* (MRSA), pose a significant global health risk because they can form biofilms that are highly resistant to standard treatments. Even with considerable progress in antibacterial materials, reliance on passive antimicrobial agents may still lead to the emergence of resistance over time. We introduce a dual-action approach by developing a gelatin/glycerol/conductive chitosan (GGCC) hydrogel that demonstrates bactericidal properties both naturally and by external stimulation. We chemically modified chitosan with unzipped CNTs to impart conductivity (~4.2 S/m) and NIR responsiveness, then blended it with gelatin to enhance its biocompatibility and skin regeneration capabilities. The antibacterial activity was enhanced via NIR (~92.23 %) and electrical stimulation (~99.85 %). Moreover, robust biofilm was also ~100 % eliminated upon electrical stimulation. To clarify the fundamental mechanisms, we performed RNA sequencing on MRSA treated with hydrogel, with and without electrical stimulation. Pathways in oxidative stress, replication, biofilm formation, and peptidoglycan synthesis were triggered, resulting in strong antibacterial and anti-biofilm properties. Electrical exposure restricts bacterial adaptability, reducing the likelihood of resistance development. Our findings indicate that integrating of conductive chitosan with electrical stimulation offers a potential, resistance-resistant approach for addressing chronic bacterial infections.

1. Introduction

Bacterial infections caused by pathogens, including *Staphylococci*, *Pneumococcus*, *Streptococci*, *Enterococci*, and *Bacillus*, are among the major public health security issues [1]. In particular, *Staphylococcus aureus*, is a leading cause of endocarditis, bacteremia, sepsis, and skin and soft-tissue infections [2]. Antibiotics have enabled the treatment of bacterial illnesses that were previously untreatable. Antibiotic treatments has enhanced the quality of life for everyone. But the rise and spread of antibiotic resistance has turned into a global public health emergency that makes the risk of illness and death much higher [3]. According to the World Health Organization, methicillin-resistant *Staphylococcus aureus* (MRSA) is one of these important pathogens that is at high risk to people [4]. MRSA is a major cause of both community- and hospital-acquired infections due to its resistance to antibiotics and robust biofilms [5]. These persistent biofilms form by releasing extracellular polymeric substances (EPS), which further prevent most antibiotics from working, thereby making this a clinical problem. These biofilms also alter the phenotype of encapsulated bacteria, leading to the growth of persistent ones [6]. Multiple or high doses of antibiotics are usually required to eradicate stubborn bacterial growth. However, overuse of antibiotics can induce severe side effects on our body, such as impairment of immune systems, kidney toxicity, digestive system disorders, and wiping out advantageous bacteria. Particularly in children, the overuse of antibiotics can increase the incidence of fatal diarrhea [7]. Long-term and excessive antibiotic use can lead to the development of new resistance mechanisms, posing a significant challenge. Given the rapid evolution of bacterial resistance and the challenge of developing novel antibiotics, we urgently need innovative strategies that think beyond conventional boundaries to combat infections caused by

* Corresponding author at: Department of Biosystems Engineering, Kangwon National University, Chuncheon, 24341, Republic of Korea.
E-mail address: ktlim@kangwon.ac.kr (K.-T. Lim).

https://doi.org/10.1016/j.ijbiomac.2025.149845
Received 25 September 2025; Received in revised form 15 December 2025; Accepted 20 December 2025
Available online 24 December 2025

resistant bacteria.

Stimuli-responsive strategies in antimicrobial treatments are helpful because they enable precise targeting and controlled release of antimicrobial agents, improve bioavailability, and potentially minimize the development of drug resistance [8,9]. These strategies leverage the ability of materials to respond to specific cues, like pH, temperature, magnetic field, electrical field, and ultrasound, to be activated or release their cargo only at the infection site or at a specific time. NIR-responsive conductive hydrogels are smart materials that can be activated by NIR light, offering a unique platform for wound healing and infection treatment. These materials show tremendous promise for treating refractory bacterial infections through ROS production, nanocatalytic therapy, and photothermal therapy [10]. However, the toxic ROS have brief lifetimes, thus leading to a limited radius of action that can only cause oxidative damage to surrounding substances. Additionally, human skin is naturally conductive with a potential difference of 10–60 mV (40–200 mV/mm) [11], seen in the epidermis. When skin is injured, the sodium (Na^+) gradient is altered, disrupting the transepithelial potential (TEP). The TEP is zero when a wound fully penetrates the epidermis, resulting in a potential gradient or an internal electric current flowing from the injured epidermis towards the wound. Hence, conductive hydrogels can help develop TEP and promote wound healing.

Chitosan is a natural, biocompatible, and biodegradable polysaccharide with broad-spectrum antibacterial activity, making it widely used in wound healing and biomedical applications [12,13]. Its cationic nature allows it to disrupt bacterial membranes; however, native chitosan suffers from key limitations such as poor solubility at neutral pH, weak mechanical properties, lack of biofilm penetration, and absence of stimuli-responsiveness for spatiotemporal effect [14,15]. These drawbacks restrict its functionality in dynamic biological environments. Moreover, its antibacterial effect is pH-dependent, diminishing under physiological conditions [16]. To overcome these limitations, chemical modification of chitosan, especially with conductive or stimuli-responsive moieties, is essential to enhance its performance in advanced applications, such as smart antibacterial hydrogels [17,18].

Here, we propose an antibacterial strategy that leverages conductive

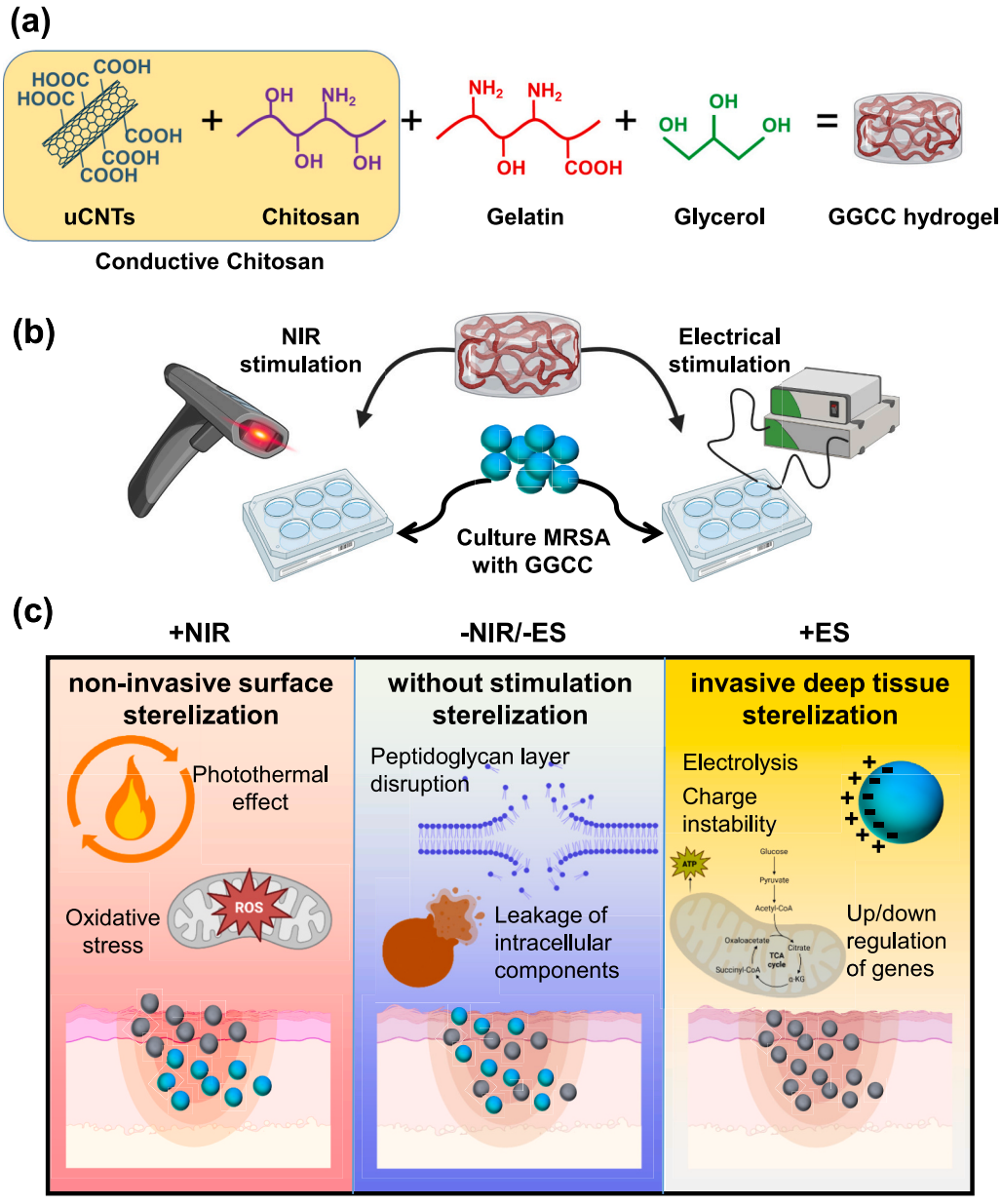

Scheme 1. Schematic representation of (a) composition and fabrication of GGCC hydrogel; (b) treatment of NIR and electrical stimulation separately for antibacterial and antibiofilm effect; and (c) overall mechanism behind the antibacterial effect with and without stimulation.

chitosan in multiple ways to treat infections, while also considering the hydrogels's biocompatibility in its native state and under stimulation. We developed a GGCC hydrogel to incorporate the biocompatibility and thermoresponsiveness of the base polymer, gelatin. Chitosan modified with uCNTs was developed to impart conductivity, NIR-responsiveness, and mechanical stability. NIR-responsive conductive chitosan, used with and without stimuli, was used to kill bacteria, overcome biofilms, and simultaneously promote the proliferation of skin cells. NIR treatment can be used for acute and surperficial infections, whereas electrical stimulation can be used for deep-tissue infections.

Additionally, the hydrogel formulation itself is highly biocompatible, and the RGD motif of gelatin can promote skin tissue regeneration. Also, the TEP hindrance caused by cell degradation can be overcome by the self-conductivity of our hydrogel. We performed RNA sequencing to identify differentially expressed genes (DEGs) in response to electrical stimulation, aiming to elucidate mechanisms underlying the effects of GGCC hydrogel with and without stimulation. The overall schematic representation of this work is presented in Scheme 1.

2. Experimental section

2.1. Materials and reagents

The following chemicals were used in the experiments: Multiwalled CNTs (MWCNTs) were received from Applied Carbon Nano (ACN, Republic of Korea). The reagents sulfuric acid (H_2SO_4) (95.0 %), hydrochloric acid (HCl) (35.0 %), and hydrogen peroxide (H_2O_2) (30 %) were purchased from Wako Chemicals (Republic of Korea). Potassium permanganate ($KMnO_4$) was purchased from Daejung Chemicals (Republic of Korea). The sodium nitrate was purchased from Sigma-Aldrich (USA). Gelatin (gel strength 300, type A, 70–90 % protein, Sigma-Aldrich, St. Louis, USA), chitosan (MW: 310–375 kDa, >75 % deacetylated, Sigma-Aldrich, St. Louis, Massachusetts, USA), and 2,2-Diphenyl-1-picrylhydrazyl (DPPH) (Sigma Aldrich, St. Louis, Massachusetts, USA) were obtained from Sigma-Aldrich. Propidium iodide and SYTO9 were purchased from Invitrogen (Seoul, Republic of Korea). WST-8 kit (Cellrix®, MediFab Co., Ltd., Seoul, Republic of Korea), human dermal fibroblasts (HDF), human epidermal keratinocytes (HaCaT), and methicillin-resistant *Staphylococcus aureus* (MRSA) were provided from the American Type of Cell Culture (ATCC) (Manassas, Virginia, USA). All chemicals were used as purchased without any additional purification.

2.2. Synthesis of uCNT, conductive chitosan, and GGCC hydrogel

Synthesis of uCNT was performed using the previously reported procedure [19]. The detailed procedure is included in Section 1.1 of the Supporting information(SI). Conductive chitosan (CC) was produced by combining uCNT with chitosan. The synthesis was performed by following a previously published protocol with modifications [20], and the detailed procedure is provided in SI section 1.2. For the development of hydrogels, required quantities of gelatin glycerol (GG) and CC solutions were individually prepared and then mixed in accordance with the ratios set out in Table S1. For GG, 2.5 mL of glycerol solution (50 %) was added in 7 mL of DI water with 1 g of gelatin. For the CC solution, the required amount of CC was prepared in 2 % acetic acid and added to the GG mixture. The synthesis of the GGCC hydrogel involved formulating a series of combinations with different ratios of G (gelatin) to CC, namely at ratios of 1:0.25, 1:0.5, and 1:1. To clarify the differences between conventional chitosan and conductive chitosan, a formulation of gelatin glycerol chitosan (GGC) was developed by adding 5 % pure chitosan to a 10 % gelatin solution (ratio 1:0.5 G:C).

2.3. Physiochemical Characterization of uCNT, CC, and GGCC

FE-SEM, FTIR, and XRD were conducted to characterize the synthesized material. The details are included in Section 1.3 of the SI. ESR was used to evaluate free radical generation from uCNT and CC with and without NIR irradiation. The rheological properties of GGCC were analyzed using a rheometer. The measurements of viscosity and shear stress were performed by varying the shear rate from 0.01 to 1000 s^{-1} at 10 °C and 37 °C. The storage modulus (G') and loss modulus (G") were measured as a function of temperature at a constant frequency of 1 Hz and a constant strain of 0.1 %.

2.4. Swelling study

To analyze the degradation of GGCC hydrogels, all freeze-dried hydrogels were immersed in 1 mL of 1 × PBS solution. Each hydrogel was removed from the 1 × PBS solution at predetermined intervals, and excess moisture was removed with tissue paper before weighing. The initial and swollen weight of the samples was recorded, and the swelling percentage was calculated using below formula:

$$W = \frac{W_i - W_t}{W_i} \times 100 \quad (1)$$

where W_i is the initial and W_t is the swollen weight of each sample.

2.5. Antioxidant activity

The ROS-scavenging activity of all hydrogels was evaluated by measuring their ability to scavenge the DPPH radical. Hydrogels with equal amounts were dipped in 0.5 mL of 0.1 mM DPPH solution and kept in the dark for 2 h. The absorbance of the samples was measured using a UV–visible spectrophotometer (Infinite® M Nano 200 Pro; TECAN, Switzerland). The antioxidant activity was calculated using the below equation:

$$\text{Antioxidant activity } (\%) = \frac{Abs_c - Abs_t}{Abs_c} \times 100 \quad (2)$$

where Abs_c is the absorbance of control (DPPH + ethanol), and Abs_t is the absorbance of treatment (sample + DPPH + ethanol).

Additionally, we performed a Terephthalic acid assay to confirm the radical-scavenging activity [21]. For this, the TA solution was mixed with Fe^{2+} and H_2O_2 to generate a radical, with/without hydrogel. After incubation, fluorescence was captured at Ex 315/Em 425 nm. A decrease in fluorescence relative to the control indicated the sample's radical-scavenging potential.

2.6. Conductivity

A multimeter and a source meter were used for the conductivity tests. The conductive properties of the hydrogels were measured from the slope of the current-voltage (IV) curves using a Sourcemeter (Keithley 2400, Keithley Instruments, Ohio, USA) at ambient temperature. Conductivity was determined using the following equation:

$$L = \frac{1}{\rho} = \frac{1}{RS} \quad (3)$$

where L is the conductivity of hydrogel, ρ is resistivity, R is the resistance, and S is the cross-sectional area. A digital multimeter (Fluke 17B+, Fluke Corporation, Washington, USA) was used to measure the resistance of a cylindrical hydrogel (2 × 1 × 0.5 cm^3) for simple resistance measurements.

2.7. Photothermal performance

The photothermal performance of GGCC hydrogels was systematically studied by irradiating 808 nm NIR light. The change in temperature was recorded over time at two power densities (1.0 W/cm^2 and 1.5 W/cm^2). The real-time temperature was recorded up to 5 min at 1 min intervals. The following formul calculated the total temperature

difference:

$$\Delta T = T_{max} - T_i \quad (4)$$

where ΔT is the temperature difference of the sample, T_{max} is the maximum temperature after irradiation of NIR light, and T_i is the initial temperature before starting the NIR exposure.

2.8. Electrical stimulation equipment

A custom-designed electrical stimulation setup was developed to apply an alternating current (AC) electric field to bacteria. A function generator (Model: Tektronix Inc., Oregon, USA) was used to deliver a controlled sinusoidal AC electric field at the desired voltage and frequency. The parameters (AC; Frequency – 25 mHz, continuous sine wave, high amplitude +250 mV, low amplitude −250 mV) were selected based on our previous report [22]. The output waveform was continuously monitored using an oscilloscope to ensure signal stability and accuracy. For stimulation, bacteria were placed in a standard 6-well plate with hydrogel. The setup and procedure are shown in the SI video. A pair of sterile platinum electrodes was inserted into each well, ensuring consistent electrode placement and uniform exposure across all samples. This setup enabled reproducible electrical stimulation under sterile conditions for in vitro experimentation. The schematic presentation and digital images of the setup are provided in Fig. 5.

2.9. In vitro antibacterial test

The surface antibacterial activity test was used to evaluate the inherent antibacterial properties of hydrogels (Gel, GG, GGC, GGCC, GGMWCNT, and GGuCNT). The MRSA was cultured in Difco™ Tryptic soy broth for growth and maintenance. Hydrogels with equal amounts were UV sterilized prior to the experiment. Bacteria were seeded with or without the hydrogels and then treated with NIR and electrical stimulation separately to assess check their bactericidal properties. For NIR treatment the culture with hydrogel was transferred to a 48-well plate and exposed to 808 nm wavelength NIR light for 10 min. After incubation of 6 h and treatment, the culture medium was diluted by serial dilution up to 10^{-4}, and 100 μL was evenly spread onto pre-prepared MacConkey agar plates. The results were confirmed using a live/dead assay with SYTO9 and PI. Antibacterial efficiency was calculated by recording the OD values and calculating according to the following equation:

$$\text{Bacteria survival rate } (\%) = \frac{OD_c - OD_t}{OD_c} \times 100 \quad (5)$$

where OD_c is the optical density of bacteria without treatment at 600 nm and OD_t is the optical density of bacteria with treatment.

For SEM image studies, the bacteria were collected by centrifugation (10,000 rpm, 5 min), washed 3 times with 1 × PBS, and dehydrated through graded ethanol solutions. The bacteria dispersed in 100 % ethanol were dropped on a cover glass slip and sputter-coated with gold for SEM imaging.

2.10. In vitro antibiofilm test

To evaluate antibiofilm activity, MRSA was cultured in tryptic soy broth and incubated in 6- and 48-well plates for 48 h to allow biofilm formation. Following incubation, the medium was carefully replaced with fresh medium containing the hydrogel, and the plates were incubated for an additional 6 h. For ES treatment, a parallel set of samples was subjected to ES during the treatment period. Whereas, for NIR treatment, 10 min was applied. A group without treatment served as the control group. After treatment, the wells were gently washed to remove planktonic bacteria, and the biofilms were stained with 0.1 % crystal violet for 15 min. Excess stain was removed by washing the wells 3 times with 1 × PBS. The stained biofilms were then visualized using an optical microscope. For quantitative assessment, the retained stain was solubilized in 33 % acetic acid, and absorbance was measured at 620 nm to determine biofilm biomass. The biofilms, treated with or without stimulation, were also analyzed using SYTO9/PI to assess the depth and extent of biofilm removal.

2.11. Transcriptomic analysis

To investigate gene expression changes in MRSA, transcriptomic analysis was conducted on bacterial suspensions treated with hydrogels in the presence or absence of ES. The detailed procedure is provided in Section 1.4 of the SI.

2.12. Biocompatibility and proliferation

Human dermal fibroblast (HDF ATCC No. PCS-201-012) cells and human epidermal keratinocytes (HaCaT ATCC No. PCS-200-011) were used to check the biocompatibility and live/dead assay. qRT-PCR was also performed to examine gene expression in the presence of GGCC hydrogels. The details of cell culture, biocompatibility, live/dead assay, and qRT-PCR are mentioned in SI section 1.5.4.

2.13. Statistical analysis

Statistical analysis was performed using OriginPro 9.0. Statistical significance between the control and treatment sets was determined using a one-way ANOVA. The data are presented as mean ± standard deviations (SDs). Differences were considered significant at $^{*}p < 0.05$, $^{**}p < 0.01$, $^{***}p < 0.001$. Non-significant difference was presented as n. s.

3. Results and discussion

3.1. Characterization of uCNT, conductive chitosan, and GGCC hydrogel

uCNT was successfully synthesized from MWCNT via a one-pot method using a previously reported protocol [23]. The uCNT was characterized using FE-SEM and FTIR, as depicted in Fig. 1a and b. At the nanoscale, uCNTs exhibit an entangled fibrous network, demonstrating their high aspect ratio and tubular structure. The MWCNT wall was partially opened by oxidation after the unzipping procedure, yielding uCNT. The morphology of uCNT is shown in Fig. 1a. The FTIR results provide compelling evidence of the chemical alterations in the conversion of MWCNT to uCNT. The vibration bands at 3402 cm^{-1} (-OH), 1707 cm^{-1} (-C=O), and 1045 cm^{-1} (C-O-C) reveal the uCNT spectra. The synthesis and characterization of uCNT is already reported in our previous article [23]. According to research, functionalized CNTs exhibit higher electroactivity compared to pristine CNTs due to the presence of oxygen-containing functional groups, specifically carboxylic acid, which enhance ion absorption and pseudocapacitive effects [24]. These functional groups facilitate stronger interactions with electrolyte ions and increase the surface area available for electrochemical reactions, thereby improving electrochemical performance. These findings confirm that incorporating uCNTs, rather than pristine CNTs, is critical for enabling electroactivity in the composite. The functional groups introduced on the CNT surface facilitate interaction with chitosan and contribute to the electrical and relaxation properties of the resulting hydrogel system.

FE-SEM, FTIR, and XRD characterized CC. As a result of the successful integration of uCNTs into the chitosan matrix, which increases surface roughness, the CC sample exhibits a rough and fragmented morphology. FTIR of chitosan, shown in Figure 1b2, revealed its functional groups [25]. The broad absorption band observed between 3000 and 3500 cm^{-1} corresponds to overlapping vibrations of hydroxyl (–OH) and amine (–NH_2) groups, which are characteristic of the polysaccharide

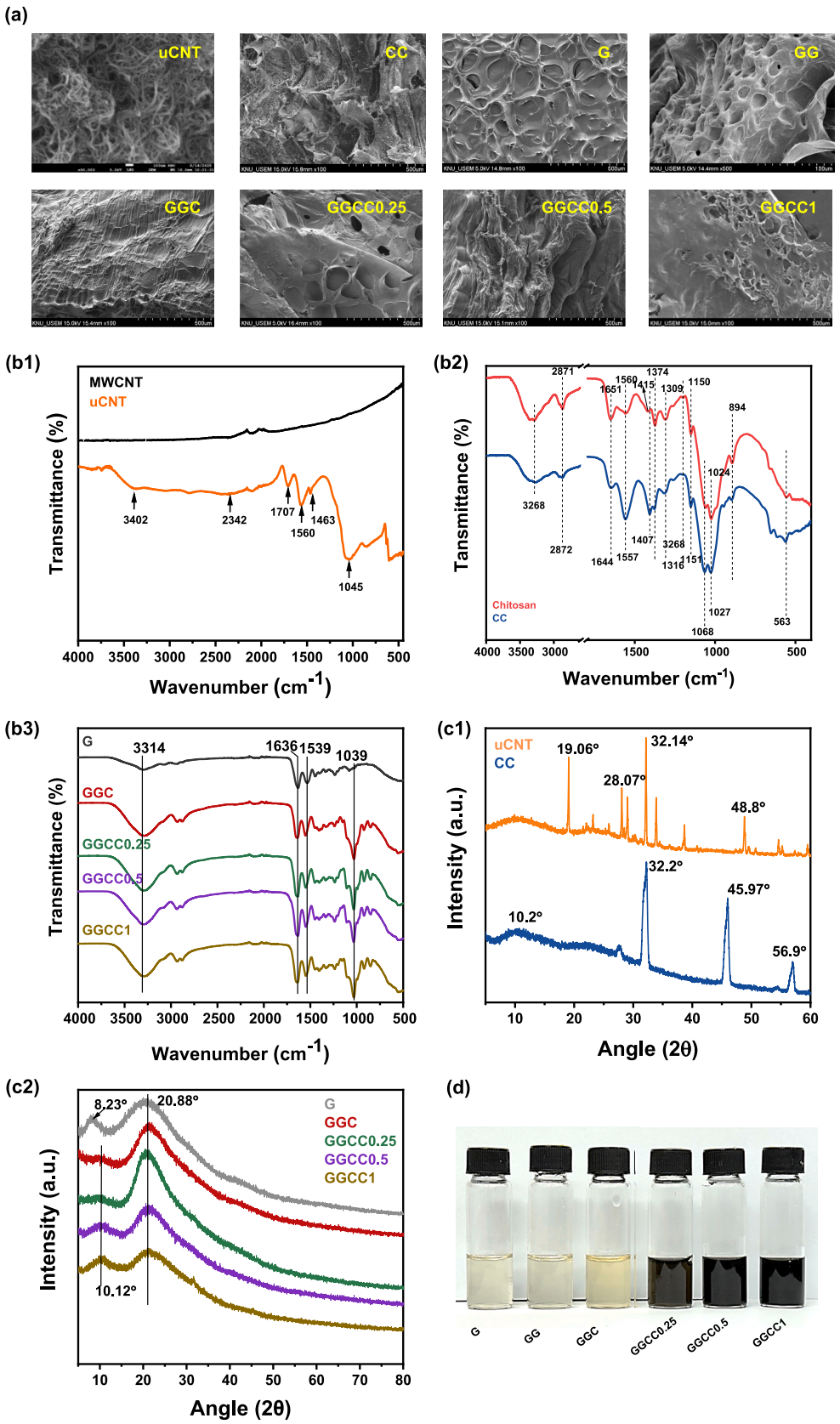

Fig. 1. Comprehensive characterization of uCNT, conductive chitosan, gelatin-based hydrogels, and GGCC composites. (a) SEM images showing microstructures of uCNT, CC, G, GG, GGC, and GGCC hydrogels with varying G to CC ratios; (b1–b3) FTIR spectra depicting functional group interactions in uCNT, CC, G, and GGCC hydrogels; (c1–c2) XRD patterns illustrating crystalline phases of uCNT, CC, and GGCC composites; (d) Digital photographs showing the macroscopic appearance and dispersion of hydrogels with increasing CC content.

backbone. The decrease in peak intensity confirms that the –OH and –NH_2 groups of chitosan were occupied in CC. The presence of a peak at 1644 cm^{-1} confirmed the amide I band, attributed to the coupling of the C═O stretching and N—H bending vibrations. Additionally, a band at 1560 cm^{-1} indicates NH_3^+ bending, while a peak at 1374 cm^{-1} is associated with amide II bands, resulting from the coupling of C—N stretching and N—H bending vibrations. The band at 1316 cm^{-1} corresponds to –OH bending, and the antisymmetric stretching of the C–O–C bond is visible at 1068 cm^{-1} and 1024 cm^{-1}, indicating the glycosidic linkages of chitosan. The FTIR spectrum of conductive chitosan, synthesized by incorporating uCNT into chitosan, showed notable changes indicative of molecular interactions between chitosan and functionalized CNTs [26].

The chemical structure and successful integration of various components in the GGCC hydrogel formulations were confirmed using SEM, FTIR spectroscopy, and XRD. SEM images of hydrogels of G and GG in Fig. 1a show a typical porous structure, with GG exhibiting greater porosity and interconnectivity due to glycerol's plasticizing properties. Because chitosan is semi-crystalline, the GGC (gelatin–glycerol–chitosan) hydrogel exhibits a more layered and compact morphology. The GGCC hydrogels exhibit notable morphological changes upon addition of CC. Whereas GGCC0.5 displays aligned, fibrous layers, most likely due to stronger molecular interactions and orientation, GGCC0.25 displays thick walls and closed pores. Curiously, GGCC1 exhibits a dense, less porous structure, indicating CC overloading that may have prevented pore formation. In general, increasing the amount of CC gradually improves structural compactness and decreases porosity, which can affect conductivity and mechanical strength.

The characteristic absorption bands of gelatin in Figure 1b3 were consistently observed in all hydrogel samples (G, GG, GGC, GGCC), with prominent peaks at 1631 cm^{-1} and 1543 cm^{-1}, corresponding to C═O stretching (amide I) and N—H bending (amide II), respectively. These bands underwent slight shifts upon modification of the hydrogel composition with glycerol, chitosan, and conductive chitosan, indicating interactions between gelatin and the added components. In all glycerol-containing hydrogels, a broad and intense absorption band in the 3700–2500 cm^{-1} region was noted, which is characteristic of O—H stretching vibrations. Additionally, a peak at 1039 cm^{-1} was observed, confirming the presence of glycerol via its C—O stretching vibration. The incorporation of chitosan and conductive chitosan introduced a new peak at 1405 cm^{-1}, which is attributed to N—H angular deformation.

Furthermore, the characteristic peaks of conductive chitosan were observed at 1642 cm^{-1} and 1540 cm^{-1}, corresponding to amide I and the NH_3^+ group, respectively. These spectral changes affirm the successful incorporation of chitosan and its conductive derivative into the hydrogel matrix. Collectively, the observed FTIR spectra confirm the successful fabrication of the GGCC hydrogel, with evidence of chemical interactions among gelatin, glycerol, and chitosan, as well as between glycerol, gelatin and conductive chitosan.

The crystalline structure and phase composition of the uCNT and the chitosan-uCNT (CC) composite were investigated using XRD analysis (Figure 1c1). The XRD pattern of uCNTs displayed a broad peak at ~19.6°, corresponding to the (002) plane with increased interlayer spacing, indicating successful oxidative unzipping and partial exfoliation of the graphitic structure. Additional peaks at 28.07°, 29.02°, 32.14°, and 33.88° suggest structural distortion and the presence of functionalized edges or defects. The minor peaks at 38.67° and 48.8° may reflect stacking irregularities or oxygenated functionalities, consistent with literature on chemically oxidized CNT derivatives.

The XRD pattern of CC showed a broad peak at ~10°, indicative of its semi-crystalline polymeric structure and consistent with the chitosan's amorphous nature. A distinct sharp peak at 27.6° was observed, which aligns with the (002) plane of graphitic carbon. This peak is slightly shifted compared to pristine CNTs (~26.4°), suggesting successful incorporation and partial restacking of unzipped CNTs within the chitosan matrix. Additional peaks at 32.2°, 45.97°, and 56.9° can be attributed to in-plane reflections, edge-plane defects, and short-range ordering, arising from structural distortion due to unzipping and chemical interactions with chitosan. These features confirm the formation of a hybrid nanocomposite with retained amorphous chitosan characteristics and embedded graphitic domains, thereby improving functionality.

The XRD patterns of the fabricated hydrogel systems reveal the structural transitions upon incorporation of chitosan and uCNTs into the gelatin matrix (Figure 1c2). Pure gelatin exhibited broad peaks at 8.23° and 20.88°, corresponding to amorphous chain packing and short-range ordering within the gelatin structure. Upon addition of chitosan and glycerol (GGC), the 20.88° peak sharpened and intensified, indicating enhanced molecular organization through hydrogen bonding. In the GGCC hydrogels, a new broad peak emerged at 10.12°, characteristic of interlayer spacing in uCNTs, confirming their successful incorporation. Simultaneously, the 20.88° peak persisted across all formulations, with improved sharpness and intensity in GGCC0.25, suggesting that lower CNT concentrations promote optimal dispersion and ordering. Higher CNT loading led to reduced peak intensity, likely due to CNT aggregation and disruption of the hydrogel network's crystalline domains. Digital images of all the fabricated hydrogels are shown in Fig. 1d.

3.2. Swelling behavior

Swelling is a property in which a polymer, such as hydrogel, undergoes volume expansion in water and increases its mass by absorbing water. The swelling behavior of materials, particularly hydrogels, is a critical factor influencing both antibacterial efficacy and biocompatibility in physiological conditions [27]. In terms of antibacterial efficacy, high swelling in an aqueous environment, such as wound exudate or bodily fluids, can be desirable, as it increases the mesh size of the polymer network, thereby facilitating rapid diffusion and sustained release of encapsulated antimicrobial agents to the target site. Conversely, excessive swelling can compromise the material's mechanical stability, leading to structural breakdown and premature loss of function, thereby limiting long-term performance, as observed in some traditional conductive hydrogels [28]. Swelling kinetics studies (Fig. 2a) of the G, GGC, and GGCC hydrogels were compared. The results indicated that, after incorporating the glycerol-chitosan composite, a dramatic change was observed. The equilibrium swelling rate of the GGCC0.5 hydrogel was significantly lower than that of pure gelatin hydrogels due to the addition of glycerol and chitosan. This balanced swelling helps GGCC hydrogels maintain long-term stability and conductivity in physiological conditions until the wound is repaired, and they degrade slowly. This also enhances biocompatibility, as the ability to swell and retain water makes a material, such as a hydrogel, highly desirable because it mimics the softness and high water content of the natural extracellular matrix (ECM), reducing the foreign body response and enhancing cell adhesion and proliferation [29]. However, the resulting hydration level and surface properties affect bioactive agent adsorption. Therefore, optimal swelling is needed. Excessive swelling can dilute beneficial surface features, while insufficient swelling may increase non-specific protein adsorption, potentially leading to inflammation or cellular toxicity.

3.3. Antioxidant assay

The DPPH (2,2-diphenyl-1-picrylhydrazyl) assay was performed to evaluate the antioxidant activity of the samples. The raw absorbance data collected for each sample is presented in Fig. 2b. The DPPH assay is based on the ability of antioxidants in the samples to reduce the stable free radical DPPH, leading to a decrease in absorbance. A lower absorbance value indicates higher antioxidant activity, as it corresponds to greater DPPH reduction. Our results indicate varying degrees of antioxidant activity among the samples based on their absorbance at 517 nm. The control, consisting solely of the DPPH radical, showed the

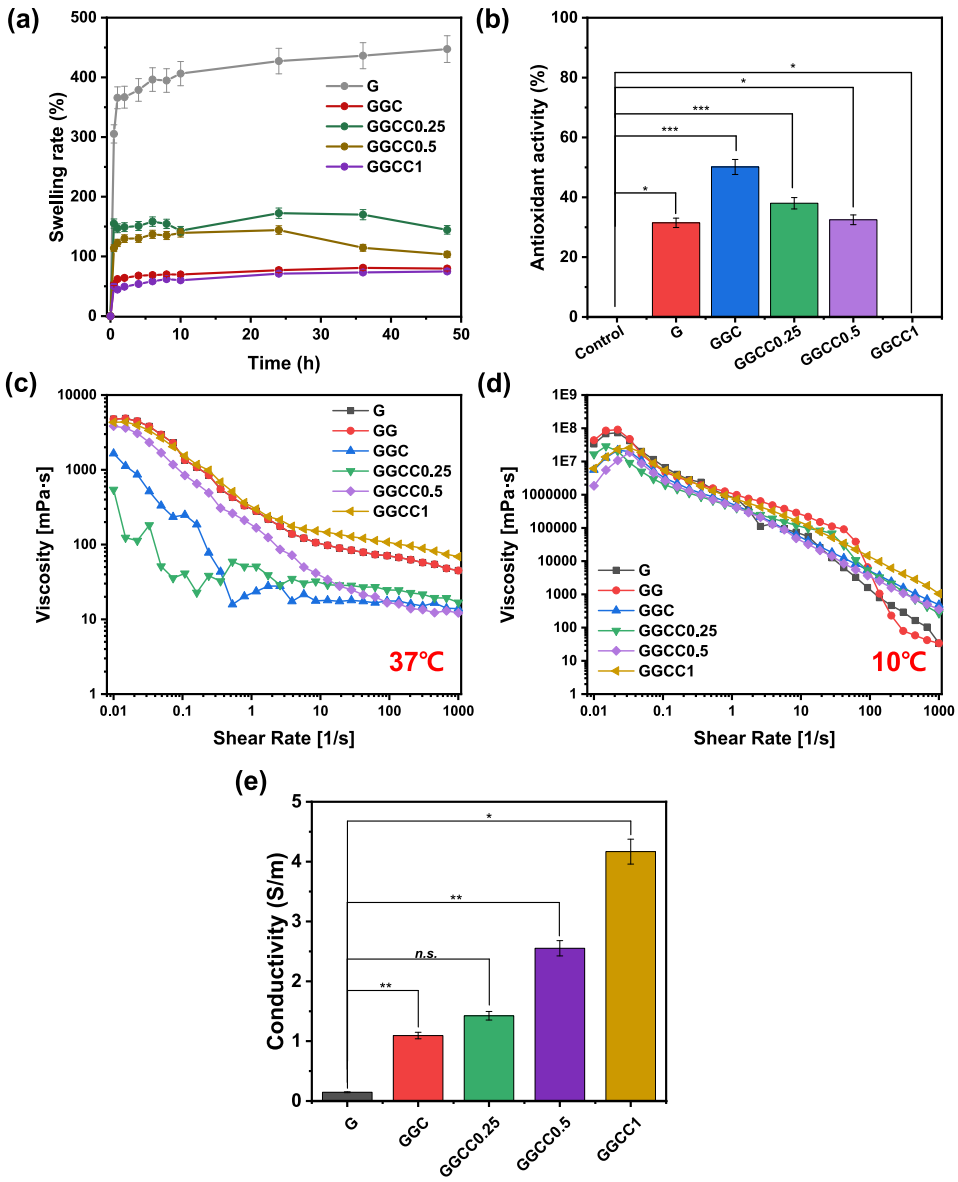

Fig. 2. Functional characterization of the hydrogels, including (a) swelling behavior over time, (b) antioxidant capacity measured by DPPH radical scavenging, (c,d) viscosity changes at room temperature (37 °C) and cold temperature (10 °C), and (e) ionic conductivity (number of replicates: $n = 4$, $^{*}p < 0.05$, $^{**}p < 0.01$, $^{***}p < 0.001$, and *n.s.*: not significant).

highest absorbance value of 0.1789, indicating minimal radical reduction and, thus, lower antioxidant activity. Sample G presented ~31 % antioxidant activity, significantly higher than the control, indicating that it possesses antioxidant properties and can effectively reduce DPPH radicals. Among the samples, GGC showed the highest scavenging activity (50 %). Conversely, samples GGCC0.25 and GGCC0.5 showed ~38 % and ~ 32 % scavenging activity, respectively. Interestingly, the sample GGCC1 showed no antioxidant activity. This suggests that adding this particular concentration may actually inhibit antioxidative properties, possibly due to a concentration-dependent effect in which higher concentrations could lead to pro-oxidative behavior.

The antioxidant assay was also measured using the terephthalic acid assay. Terephthalic acid reacts with hydroxyl radicals (·OH) generated by the Fenton reaction to form fluorescent 2-hydroxylterephthalic acid (HTA). In the presence of free radicals, ·OH is scavenged, reducing HTA fluorescence formation. Fig. S2 shows the fluorescent images of the HTA after incubation for 20 mins. The outcomes shown in Fig. S2 are consistent with the DPPH assay, which confirms that GGC, GGCC0.25, and GGCC0.5 showed scavenging activity.

3.4. Rheology

To evaluate the rheological behavior and temperature stability of the developed hydrogels, viscosity measurements were performed at physiological (37 °C) and low (10 °C) temperatures (Fig. 2c,d). All formulations demonstrated shear-thinning behavior, characteristic of physically crosslinked polymeric systems suitable for injectability. At 37 °C, G and GG hydrogels exhibited high initial viscosity but dropped sharply under increasing shear, indicating lower mechanical stability. Incorporation of chitosan (GGC) and CC (GGCC0.25–GGCC1) led to enhanced and more stable viscosity profiles, with GGCC1 maintaining the highest viscosity across the shear range. At 10 °C, all samples showed increased viscosity due to reduced chain mobility; however, GGCC hydrogels, particularly GGCC1, exhibited consistent shear-dependent behavior, suggesting excellent thermal resilience and potential freeze stability. The inclusion of glycerol played a vital role in modulating the network flexibility and hydration, acting as a plasticizer and improving low-temperature performance. In contrast, the uCNT–chitosan network reinforced structural integrity across a range of temperatures. The

adhesive properties of hydrogels on the skin are demonstrated in Fig. S1, which shows the stability of the hydrogel on the skin surface.

3.5. Conductivity

The electrical conductivity of the hydrogels was evaluated using a probe method, and the results are presented in Fig. 2e. A progressive increase in conductivity was observed with the incorporation of uCNTs. The pristine gelatin hydrogel exhibited minimal conductivity (~0.1 S/m), whereas the addition of chitosan (GGC) increased it to ~1.1 S/m. Further doping with uCNTs resulted in a dose-dependent enhancement in conductivity: GGCC0.25, GGCC0.5, and GGCC1 exhibited conductivities of ~1.4 S/m, ~2.5 S/m, and ~ 4.2 S/m, respectively. This significant improvement can be attributed to the excellent electrical properties of uCNTs, which formed conductive pathways throughout the hydrogel matrix. The interconnected network of uCNTs facilitated efficient electron transport, thereby reducing the overall resistance. The corresponding resistance values decreased from 419 kΩ (G) to 14.7 kΩ (GGCC1), corroborating the conductivity data. These findings highlight the tunable conductivity of the GGCC hydrogels, which is crucial for applications such as electrically responsive wound dressings and tissue engineering scaffolds where electrical stimulation can promote cellular responses and healing.

3.6. NIR responsiveness of GGCC hydrogels

The photothermal response of the GGCC hydrogels under NIR irradiation was investigated at two power densities: 1.0 W/cm^2 (Fig. 3a) and 1.5 W/cm^2 (Fig. 3b). A time-dependent and concentration-dependent increase in temperature was observed for all GGCC formulations. At both intensities, GGCC1 showed the greatest temperature increase, reaching approximately 100 °C within 5 min at 1.5 W/cm^2, while lower concentrations (GGCC0.25 and GGCC0.5) showed intermediate heating behavior. In contrast, G, GG, and GGC hydrogels showed negligible temperature rise (<35 °C), indicating the necessity of uCNT incorporation for photothermal efficiency. This enhanced photothermal behavior is attributed to the strong NIR absorption and heat-conversion ability of the uCNTs embedded within the hydrogel matrix. The photothermal images of the increase in temperature due to NIR irradiation at varying power densities are presented in Fig. 3c. It shows the total temperature difference of hydrogels after NIR exposure. The photothermal effect is particularly relevant for potential antibacterial applications, where localized heating can eradicate pathogens or biofilms. To further investigate the NIR-mediated ROS generation, ESR spectroscopy was performed. As shown in Fig. 3d and e, both uCNT and CC demonstrated a significant ROS signal under NIR irradiation (green lines).

In contrast, negligible signals were observed in the absence of NIR (purple lines). The characteristic ESR peaks confirm the formation of singlet oxygen or other radical species upon irradiation, implying that the material possesses intrinsic photoactive properties. The dual ability of the GGCC hydrogel system to convert NIR light into localized heat and to simultaneously generate ROS makes it a promising platform for combining photothermal and photodynamic therapy. These properties are particularly advantageous for wound healing and antibiofilm applications, where both heat and oxidative stress can effectively disrupt microbial viability.

For further experiments we used the GGCC0.5 group, considering the multifunctional properties. GGCC0.5 achieved the best quantitative balance across all critical performance metrics compared to GGCC0.25 and GGCC1. Specifically, GGCC0.5 exhibited optimal swelling properties and mechanical stability, making it a suitable candidate for a stable dressing. It provided optimum antioxidant scavenging activity (~32 % DPPH scavenging efficiency), which is crucial for mitigating damaging ROS during the initial inflammatory phase of wound healing, whereas GGCC1 showed negligible activity. Furthermore, GGCC0.5 exhibited an optimal electrical conductivity (~2.5 S/m), sufficient for effective electrical stimulation, thereby avoiding the low conductivity of GGCC0.25. Most importantly for safety, GGCC0.5 demonstrated an acceptable photothermal response, reaching a maximum temperature of ~50 °C under NIR exposure, which is sufficient for bacterial killing but safely below the threshold for damaging surrounding healthy cells, a significant risk with the excessively high photothermal activity of GGCC1. Thus, GGCC0.5 represents the best formulation that simultaneously ensured stability, effective electrochemical function, sufficient antioxidant capacity, and crucial photothermal cytocompatibility.

3.7. Antibacterial and antibiofilm assay

3.7.1. Antibacterial efficacy of GGCC hydrogels under NIR stimulation

To evaluate the combinatorial antibacterial efficacy of the GGCC hydrogels, a schematic illustration (Fig. 4a) highlights the synergistic mechanism in which NIR-triggered photothermal and ROS activities

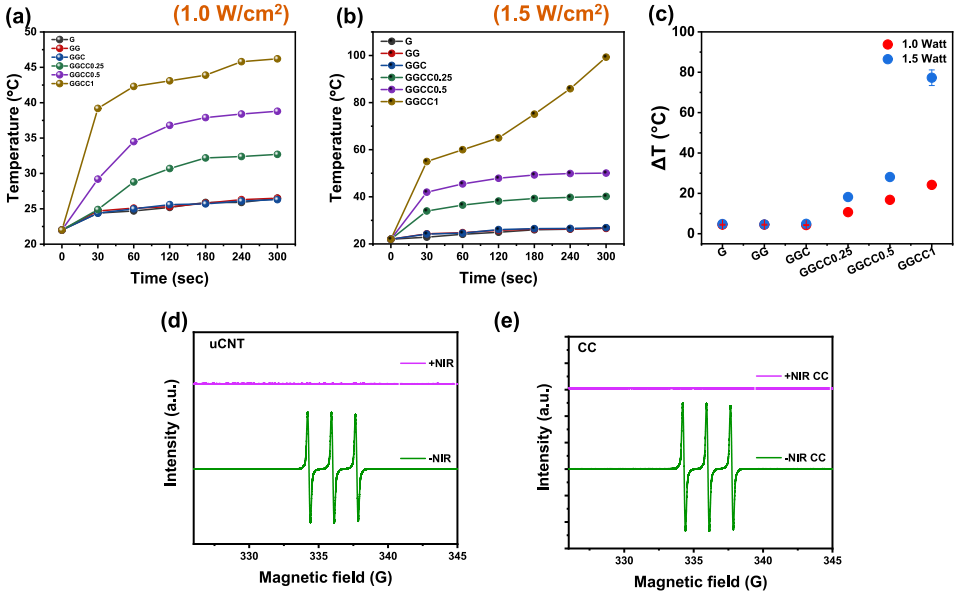

Fig. 3. Photothermal effect of NIR of hydrogel at (a) 1.0 W/cm^2 and (b) 1.5 W/cm^2 and (c) their temperature difference at both power densities, generation of ROS from synthesized (d) uCNT and (e) conductive chitosan.

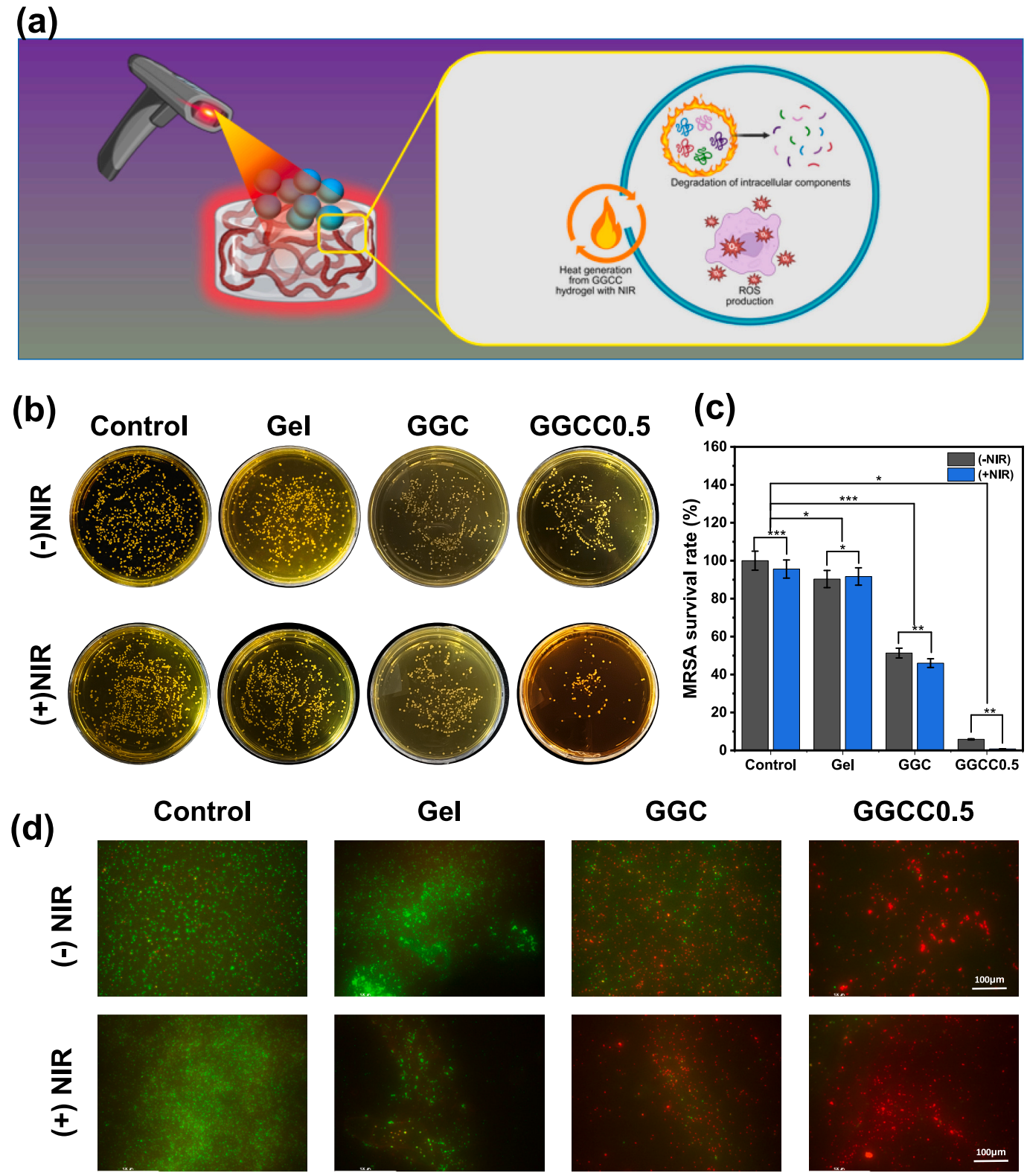

Fig. 4. Antibacterial activity of hydrogel in presence of NIR stimulation (a) schematic presentation, (b) agar plates showing antibacterial effect, and (c) their respective antibacterial efficiency (d) Live/dead assay (number of replicates: $n = 4$, $^{*}p < 0.05$, $^{**}p < 0.01$, $^{***}p < 0.001$, and *n.s.*: not significant).

disrupt bacterial membranes. The antibacterial efficacy was quantified by CFU assays for *S. aureus* (Fig. 4b) with and without NIR exposure. The untreated and GGC-treated groups showed substantial bacterial growth, whereas the GGCC0.5 hydrogel under NIR irradiation exhibited a drastic reduction in bacterial colonies, demonstrating its potent photothermal-mediated antibacterial activity. Quantitative CFU analysis confirmed this trend, with GGCC0.5-NIR resulting in an ~84.18 % reduction in viable bacteria compared to controls. A similar trend was observed for MRSA (+NIR), with the GGCC0.5 + NIR group exhibiting significantly greater antibacterial efficacy (~95.23 %) than groups without NIR or uCNT. This highlights the relevance of photoresponsive components in tackling antibiotic-resistant strains.

The antibacterial activity of different hydrogels under NIR irradiation was evaluated for pure MWCNT and uCNT-incorporated GG hydrogels (Fig. S3a). Compared with the control, all hydrogel groups showed reduced bacterial colonies, with GGCC0.5 exhibiting the most pronounced antibacterial effect. Quantitative analysis based on OD values (Fig. S3b) revealed a significant decrease in bacterial survival rate upon NIR stimulation, particularly in the GGMWCNT and GGCC0.5 groups, confirming the synergistic effect of photothermal heating with conductive components. These results demonstrate that the incorporation of alone, unzipped CNTs does not have an antibacterial effect. Hence, the fabricated conductive chitosan enhances the photothermal antibacterial efficiency. The superior activity of GGCC0.5 is attributed to its optimal conductivity and photothermal conversion, which effectively disrupt bacterial viability and biofilm formation.

Live/dead fluorescence imaging of MRSA biofilms (Fig. 4d) further validated these findings. Control and GGC-treated samples showed

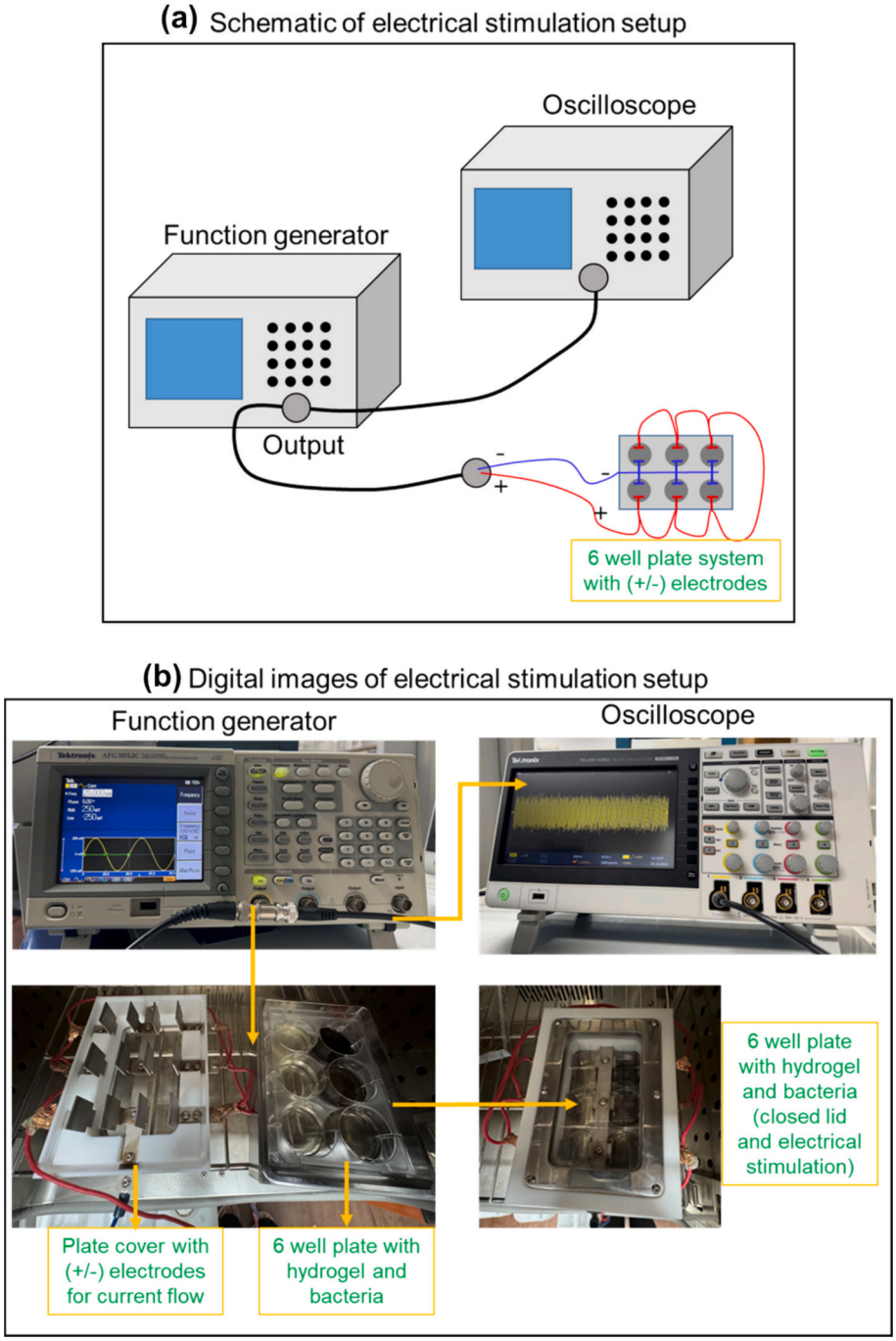

Fig. 5. Electrical stimulation setup (a) schematic presentation (b) digital images and the flow of setup.

dense green fluorescence, indicating the presence of live bacterial biofilms. In contrast, the GGCC0.5 + NIR group showed prominent red fluorescence, indicating a substantial increase in dead bacteria. The diminished green signal and intensified red staining reflects the effective penetration of the sample and disruption of MRSA via localized heating and ROS generation. These results collectively confirm the GGCC hydrogel's synergistic antibacterial effects under NIR stimulation. This dual-action platform is particularly advantageous in clinical wound care, where drug-resistant pathogens are major challenges.

3.7.2. Antibacterial efficacy of GGCC hydrogels under electrical stimulation

To investigate the impact of ES on antibacterial performance, the hydrogels were subjected to ES (Fig. 5a, b) using a custom setup with a possible mechanism (Fig. 6a). Agar plate images (Fig. 6b) demonstrated that in the absence of ES, bacterial colonies were abundant in the control, G, and GGC groups, while GGCC0.5 exhibited moderate antibacterial activity. Upon application of ES, a marked reduction in bacterial colonies was observed, especially in the GGCC0.5 group, indicating the synergistic effect of conductive hydrogel and electrical stimulation. Quantitative CFU analysis (Fig. 6c) confirmed these results, showing a substantial decrease in bacterial count for the GGCC0.5 + ES group compared to other samples. This suggests that electrical stimulation effectively enhances the antibacterial performance of GGCC0.5 hydrogel, likely due to increased membrane disruption, electroporation, penetration of GGCC components, and electrochemical stress on the bacterial cells. Live/dead fluorescence imaging (Fig. 6d) further validated the enhanced antibacterial effect. In the absence of ES, the control and G/GGC groups exhibited predominantly green fluorescence (live bacteria), while GGCC0.5 showed a mixed population. Upon ES, GGCC0.5-treated samples showed intense red fluorescence (dead bacteria), confirming effective bacterial inactivation under combined electrical and material-based stimuli. SEM imaging (Fig. 6e) revealed significant morphological changes and membrane rupture in bacterial cells. In the absence of ES, bacteria retained their intact spherical morphology. However, post-ES treatment, especially in the GGCC0.5 group, bacterial cells appeared deformed, shriveled, or lysed, indicating membrane disruption and structural collapse due to electrical stress in combination with conductive hydrogel contact. These results highlight the potent antibacterial properties of GGCC0.5 hydrogels under ES. The presence of CC not only facilitates current conduction but also promotes localized membrane stress, leading to efficient bacterial eradication. This makes GGCC hydrogels a promising platform for smart wound dressings, particularly in chronic or infected wounds where bacteria are often resistant to conventional treatments.

The antibacterial performance of hydrogels containing only MWCNT and uCNTs with GG was performed under electrical stimulation as shown in Fig. S4a. Upon ES application, a marked reduction in MRSA colonies was observed, especially in the GGCC0.5 hydrogel group. The quantitative survival data (Fig. S4b) indicated a significant decrease in bacterial viability under ES compared to non-stimulated controls, highlighting the potent antibacterial role of electrical signals with GGCC0.5 hydrogel. These findings confirm that conductive chitosan is more antibacterial than pure MWCNT or uCNTs. Also, electrical stimulation not only amplifies the inherent antibacterial activity of conductive hydrogels but also provides a promising strategy for combating resistant and persistent bacterial infections.

3.7.3. NIR-stimulated biofilm eradication by GGCC hydrogels

To assess the antibiofilm capability of the developed hydrogels, crystal violet staining was used to visualize and quantify biofilm biomass before and after NIR irradiation. As shown in Fig. 7a, dense and dark biofilm clusters were observed in the untreated control and G groups under both -NIR and + NIR conditions, indicating limited biofilm disruption. GGC showed marginal reduction in biofilm density, but the most notable reduction was observed in the GGCC0.5 group under NIR stimulation, where minimal biofilm remnants remained, suggesting effective biofilm dispersal and bacterial killing. The confocal images presented in Fig. 7b also show and confirm the removal of biofilms in the presence of GGCC0.5 hydrogel. In addition, with the NIR eradication, the CLSM image showed high dead (PI) stain, which confirms the effect of killing of bacteria and biofilm. Quantitative analysis of biofilm biomass through OD_{620} measurements (Fig. 7c) supported these observations. The GGCC0.5 + NIR group exhibited the lowest OD values, signifying maximum biofilm eradication. Compared to NIR (−) samples, all NIR (+) groups showed a trend of reduced OD, with the GGCC hydrogel exhibiting the highest sensitivity and responsiveness to NIR light. The schematic (Fig. 7d) illustrates the proposed mechanism, where GGCC hydrogel, upon NIR exposure, generates localized heat and ROS via CC. These dual photothermal and oxidative mechanisms effectively penetrate and disrupt the EPS matrix of biofilms, leading to microbial membrane damage and enhanced biofilm clearance. These findings emphasize the potential of GGCC hydrogels as a smart, light-responsive platform capable of combating persistent biofilms, a major challenge in chronic wound management and implant-related infections. The ability to precisely activate antibacterial effects using external light adds a layer of control for therapeutic interventions.

3.7.4. ES-stimulated biofilm eradication by GGCC hydrogels

To investigate the antibiofilm efficacy of the hydrogels under ES, biofilm biomass was evaluated using crystal violet staining and quantified via OD_{620} measurements (Fig. 8a, c). In the absence of ES (–ES), the control and G hydrogel groups exhibited dense, well-established biofilm networks, as indicated by intense crystal violet staining. Moderate biofilm disruption was observed with GGC and GGCC0.5 even without stimulation, likely due to their inherent antimicrobial properties. Upon application of ES, all hydrogels demonstrated visibly enhanced biofilm clearance, with the GGCC hydrogel exhibiting the most pronounced reduction in retained stain, indicating substantial biofilm eradication. Fig. 8b displays CLSM images that corroborate the eradication of biofilms in the presence of GGCC0.5 hydrogel. Furthermore, following the elimination of ES, the CLSM picture exhibited significant red (PI) staining, hence corroborating the bactericidal and biofilm eradication effects. This effect was quantitatively supported by OD analysis (Fig. 8c). The control and G groups maintained high OD values in the absence of ES, while GGC and GGCC showed moderately reduced values. Following ES, a marked decline in OD was observed across all samples, with GGCC0.5 + ES achieving the lowest biofilm biomass. This underscores the significant contribution of conductive fillers—uCNTs and chitosan—in amplifying the electrical stimulation effect. The proposed mechanism is illustrated in Fig. 8d, where ES delivered through the conductive hydrogel matrix generates a localized electric field that disrupts the EPS and weakens bacterial adhesion. This physical disruption, combined with potential electrochemical stress, results in effective biofilm detachment and bacterial inactivation. Together, these findings highlight the critical role of ES in enhancing antibiofilm performance. The GGCC hydrogel, particularly under ES, emerges as a powerful dual-functional platform capable of dismantling resilient biofilms through integrated electrical, mechanical, and chemical mechanisms, making it highly suitable for chronic wound applications where biofilm persistence hinders healing.

3.8. Transcriptomic analysis of (+/-ES) GGCC-treated MRSA

To visualize the global transcriptional shifts induced by hydrogel treatment with and without ES, scatter plots were generated comparing gene expression levels between the groups (Fig. 9a). In the comparison between hydrogel without electrical stimulation (−ES GGCC0.5) and the control, a substantial number of genes showed altered expression, with many upregulated (red dots) and downregulated (green dots) transcripts, indicating the hydrogel's intrinsic antibacterial activity. When the hydrogel was applied with electrical stimulation (+ES GGCC0.5)

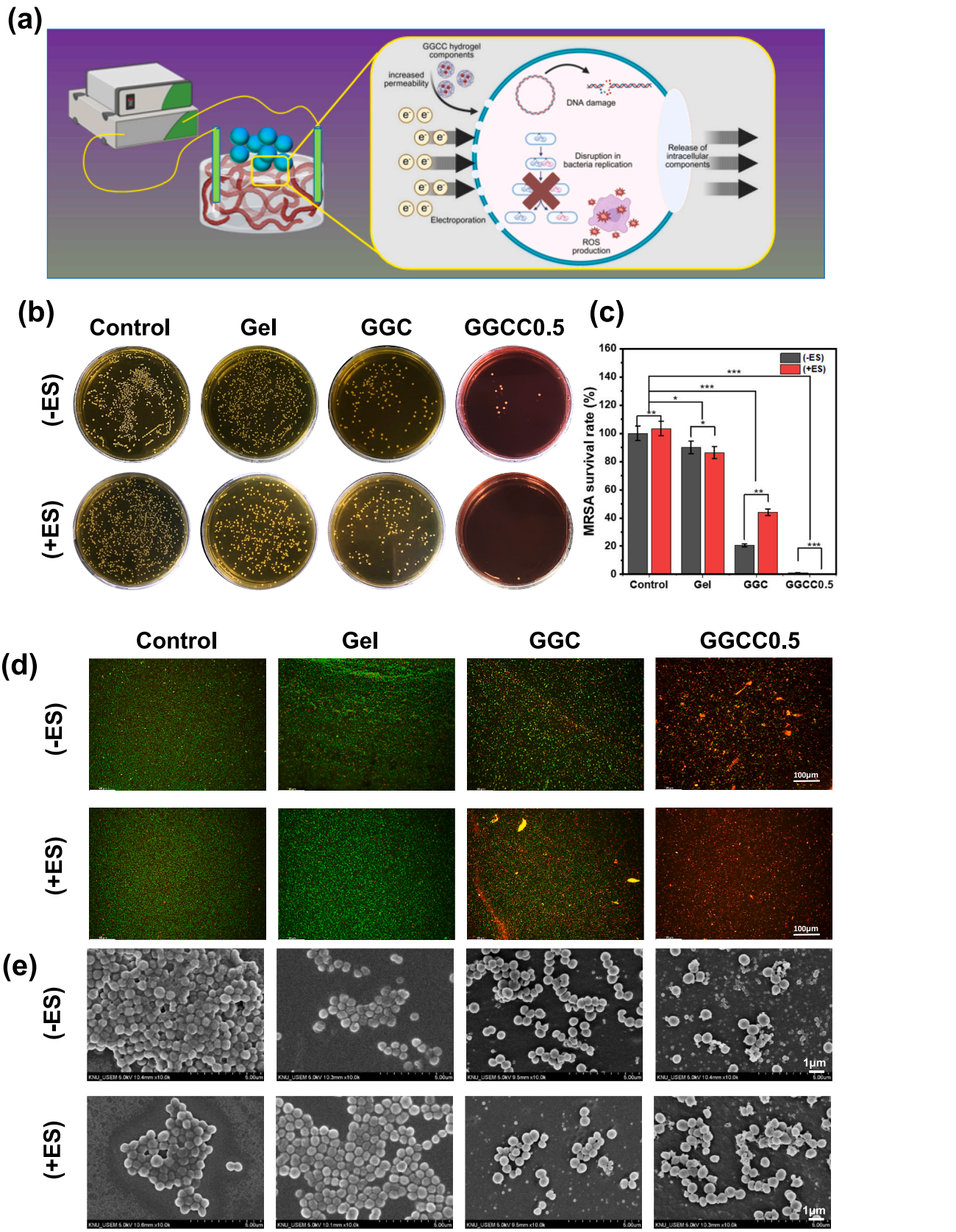

Fig. 6. Antibacterial activity of hydrogel in the presence of electrical stimulation (a) schematic presentation, (b) agar plates showing antibacterial effect and their respective (c) antibacterial efficiency, (d) live/dead assay, and (e) SEM images (number of replicates: $n = 4$, $^{*}p < 0.05$, $^{**}p < 0.01$, $^{***}p < 0.001$, and *n.s.*: not significant).

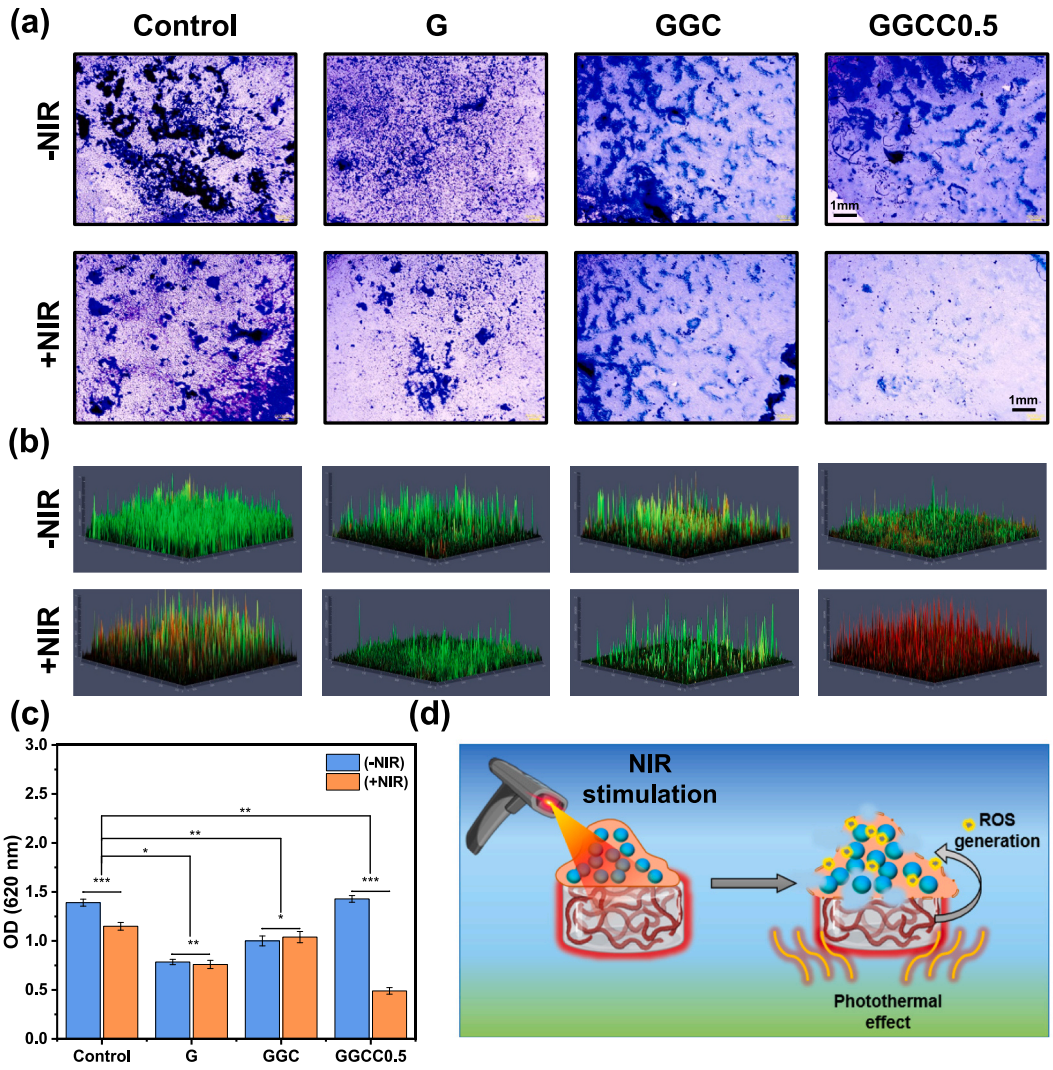

Fig. 7. Effect of NIR stimulation on biofilm eradication (a) microscopic images of crystal violet staining, (b) confocal images of (SYTO9/PI) stained biofilms, (c) their OD values of retained stain, and (d) schematic presentation of NIR stimulation and effect on biofilm eradication (number of replicates: $n = 4$, $^{*}p < 0.05$, $^{**}p < 0.01$, $^{***}p < 0.001$, and *n.s.*: not significant).

versus control, a similar but more pronounced deviation from the diagonal was observed, suggesting an amplified transcriptional response. Notably, the direct comparison between +ES GGCC0.5 and − ES GGCC0.5 revealed a distinct subset of differentially expressed genes (DEGs), confirming that ES introduces a unique modulatory effect on bacterial gene expression. Overall, these scatter plots highlight the transcriptomic effects of the hydrogel and underscore the synergistic or additive role of ES in regulating bacterial gene expression. To decode the transcriptional responses of MRSA to the GGCC0.5 hydrogel and its ES, we conducted differential gene expression analysis across three conditions: hydrogel without electrical stimulation (-ES GGCC0.5) vs. control, hydrogel with electrical stimulation (+ES GGCC0.5) vs. control, and + ES GGCC0.5 vs. -ES GGCC0.5. A Venn diagram analysis (Fig. 9b) revealed that 56 genes were contra-regulated across all three comparisons, suggesting a core set of genes upregulated/downregulated by the GGCC0.5 treatment, irrespective of electrical stimulation. Treatment with the hydrogel alone (-ES GGCC0.5 vs. control) resulted in 90 genes uniquely upregulated and 73 uniquely downregulated, indicating a distinct transcriptomic shift induced by the material.

In contrast, +ES GGCC0.5 vs. control induced 75 genes uniquely upregulated and 51 uniquely downregulated, highlighting the additional modulatory impact of electrical cues. Furthermore, the direct comparison between +ES and -ES with hydrogel identified 10 genes uniquely upregulated and 15 uniquely downregulated, confirming that electrical stimulation introduces a unique layer of gene regulation. The overlapping set of 303 upregulated and 336 downregulated genes between both hydrogel-treated groups -ES and + ES GGCC0.5 vs. control, likely represents the core antibacterial response induced by the hydrogel system. These findings collectively suggest that while the GGCC0.5 itself significantly disrupts the MRSA transcriptome, the application of electrical stimulation further enhances and diversifies the bacterial gene expression profile, potentially amplifying the antimicrobial efficacy.

Principal Component Analysis (PCA), shown in Fig. 9d, was performed to assess the global variance in gene expression profiles across treatment groups. The PCA plot clearly demonstrates distinct clustering of samples corresponding to the control (red), −ES GGCC0.5 (blue), and + ES GGCC0.5 (green). The first two principal components (PC1 and PC2) accounted for 72.39 % and 27.61 % of the total variance, respectively, highlighting strong treatment-dependent transcriptomic shifts. The separation along PC1 primarily distinguishes GGCC-treated samples from the control, while PC2 further differentiates the +ES and − ES hydrogel groups, indicating that ES contributes an additional layer of gene expression modulation. Specific genes contributing to the variance, such as *recA*, *metG*, and *DQM91_RS0525,* were associated with key pathways including DNA repair, metabolic regulation, and stress response. This clear stratification reinforces that both the GGCC0.5 and

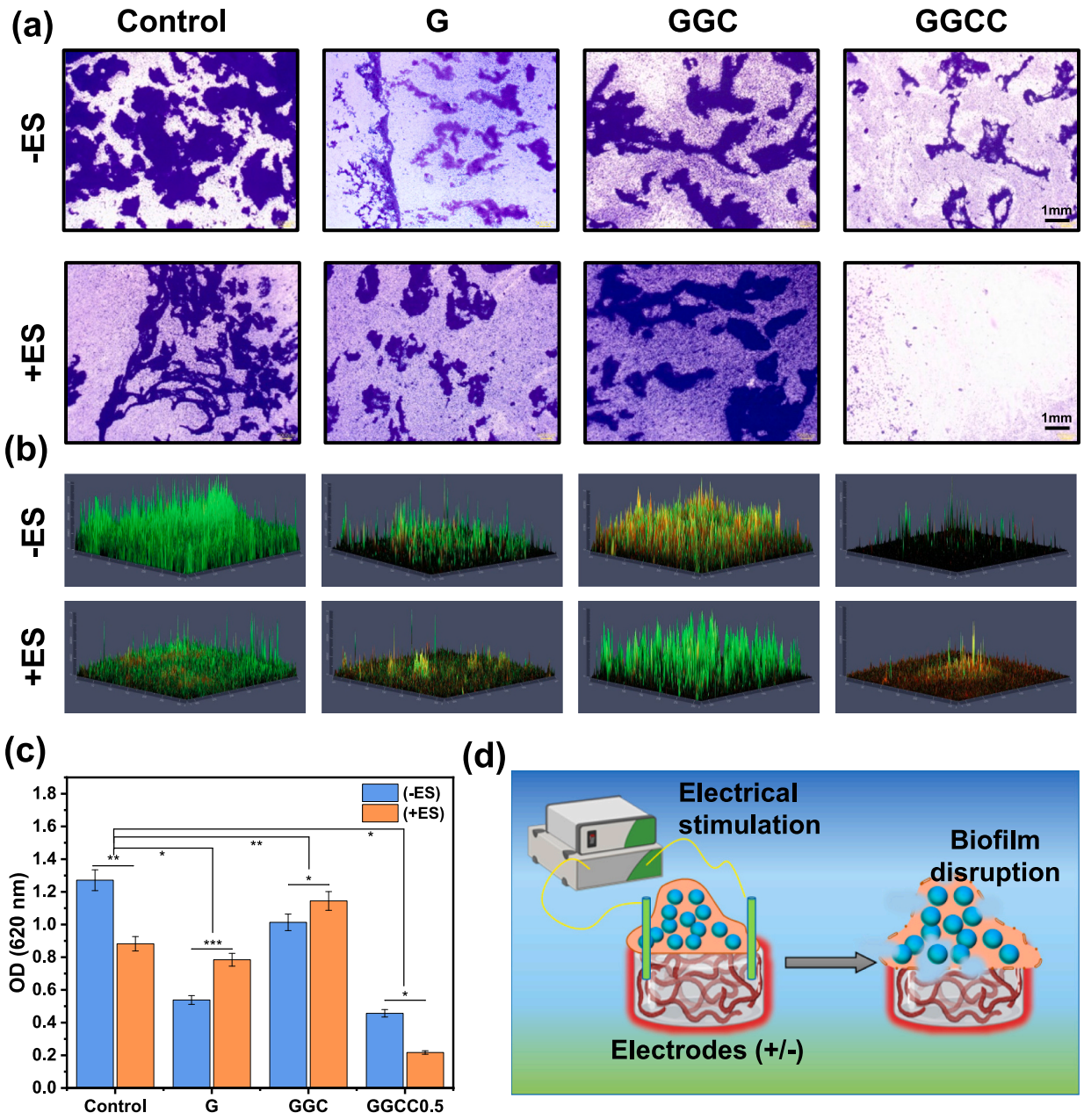

Fig. 8. Effect of electrical stimulation on biofilm eradication (a) Microscopic images of crystal violet staining, (b) confocal images of (SYTO9/PI) stained biofilms, (c) their OD values of retained stain, and (d) schematic presentation of electrical stimulation and effect on biofilm eradication (number of replicates: $n = 4$, $^{*}p < 0.05$, $^{**}p < 0.01$, $^{***}p < 0.001$, and *n.s.*: not significant).

ES independently and synergistically influence the bacterial transcriptome, offering mechanistic insight into their antibacterial efficacy.

To unravel the underlying molecular mechanisms responsible for the antibacterial efficacy of +ES GGCC0.5, RNA sequencing was performed. Fig. 10a and c present the heatmaps and network-level analysis of key functional gene categories, offering deep insights into the bacterial stress response. Heatmap analysis of cell division-associated genes showed significant downregulation of *ftsZ*, *murB*, *zapA*, and *ftsA* under +ES GGCC0.5 treatment, indicating inhibition of bacterial proliferation. This suggests that the electroactive GGCC hydrogel disrupts essential division machinery, contributing to reduced viability and colony-forming units. Genes linked to biofilm formation (*purN, icaA, ligA, sfaA*) were notably downregulated in the +ES and -ES groups compared to the control. This transcriptional suppression correlates with experimental findings (Fig. 8), where ES-treated GGCC samples showed significant biofilm eradication. The reduction of *ligA* and *sfaA* implies weakened biofilm structural integrity and adhesion capacity. ROS metabolism genes, including *ahpC*, *ahpF*, and *trxB*, were significantly upregulated under +ES conditions compared to -ES, indicating elevated oxidative stress within bacterial cells. This matches the ROS detection via ESR (Fig. 3), confirming the generation of intracellular oxidative stress that likely contributed to bacterial membrane damage and death.

For further understanding of the effect of ES compared to –ES, we explored the significance of key gene markers related to cell division and peptidoglycan synthesis, including *ftsA*, *ftsW*, *ftsL*, *ezrA*, *zapA*, *mraY*, and *murC*. In bacterial cell division, the divisome is a protein complex accountable for cell division [30]. *ftsA*, *ftsW*, and *ftsL* play important roles in the assembly and function of the divisome. The downregulation of these genes in +ES vs. -ES indicates an interrupted division. The filamentous temperature-sensitive mutant Z (*ftsZ*) allows the formation of the *Z*-ring, which works as a scaffold for division and aids in the recruitment of division-related proteins [31]. The gene *zapA* enables the

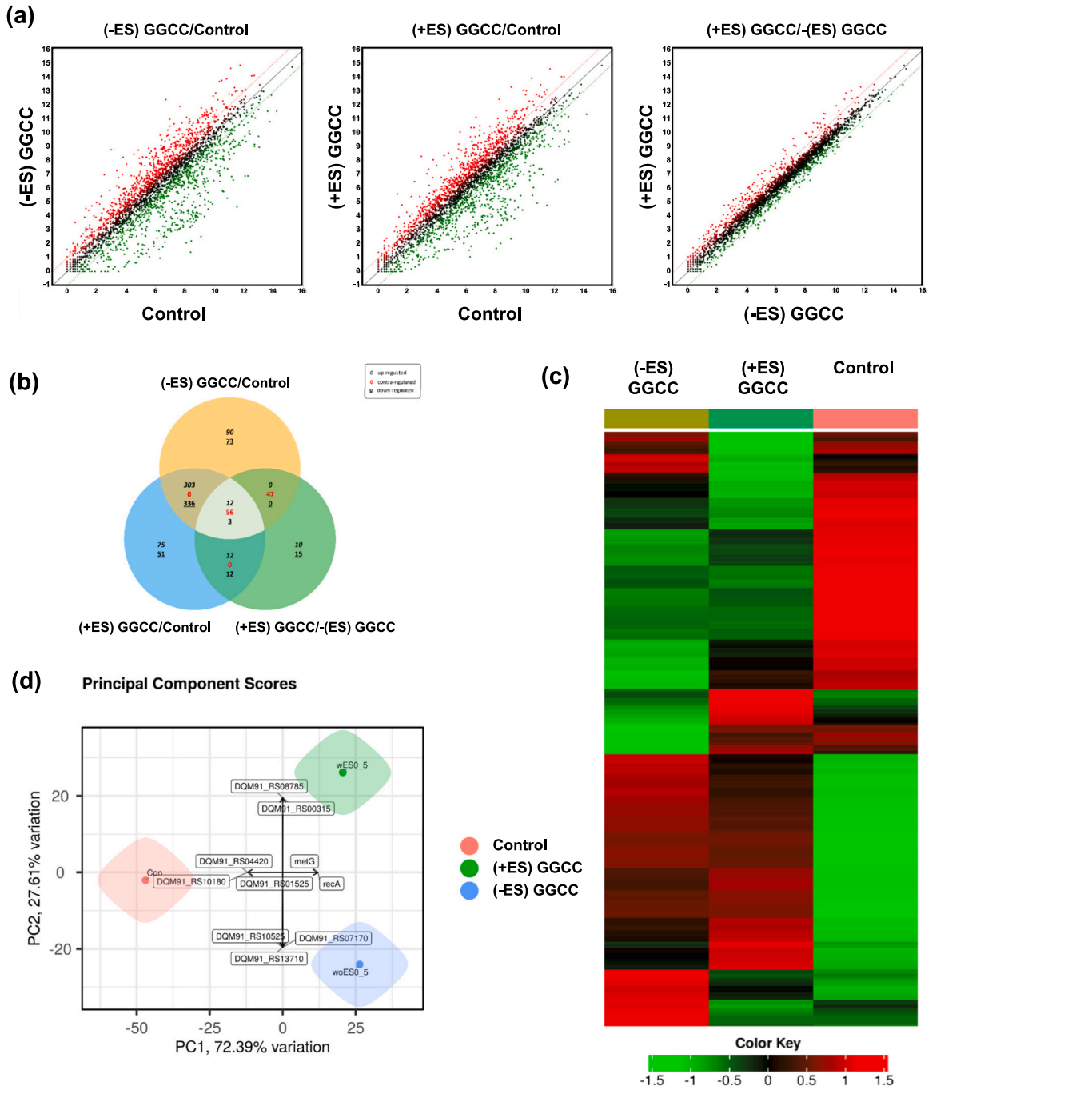

Fig. 9. Transcriptomic analysis for hydrogel and stimulation effect on MRSA (a) scatter plot, (b) Venn diagram, (c) heatmap of control –ES GGCC0.5, and + ES GGCC0.5 and (d) principal component scores.

stabilization and functionalization of the Z-ring, and *ezrA* regulates it, ensuring its proper organization. It also prevents the improper assembly of the Z-ring [32,33]. Similarly, peptidoglycan biosynthesis-related genes, including *mraY* and *murC*, which are required for peptidoglycan biosynthesis, were also downregulated, suggesting a complete cessation of cell wall synthesis [34,35]. Hence, transcriptomic analysis of DEGs revealed that ES induces transcriptional alterations in MRSA that suppress replication and cell wall synthesis, contributing to the antibacterial effect.

Biofilms are populations of bacteria affixed to a substrate and encased in an extracellular matrix [36]. The *typA* and *prfA* were upregulated in the presence of GGCC0.5 compared to the control. The *typA* functions for GTPase regulating the ribosome function in stress enable biofilm formation, and it also leads to the attachment of bacteria to the surface [37]. *prfA* is a crucial transcription factor that promotes the transcription of multiple virulence genes and governs the transition of bacteria from extracellular to intracellular state [38]. The key biofilm regulatory genes and stress-related genes, including *rpoZ, sarA, pde2, mazE,* and *purN*, were found to be downregulated in the group treated with ES compared to -ES GGCC0.5. The *rpoE* gene encodes for RpoE protein, a sigma factor that binds to RNA polymerase, and forms a holoenzyme, which further directs the transcription of stress related genes and further promotes biofilm formation [39]. The *rpoZ* gene encodes for the omega subunit of RNA polymerase which further leads to the

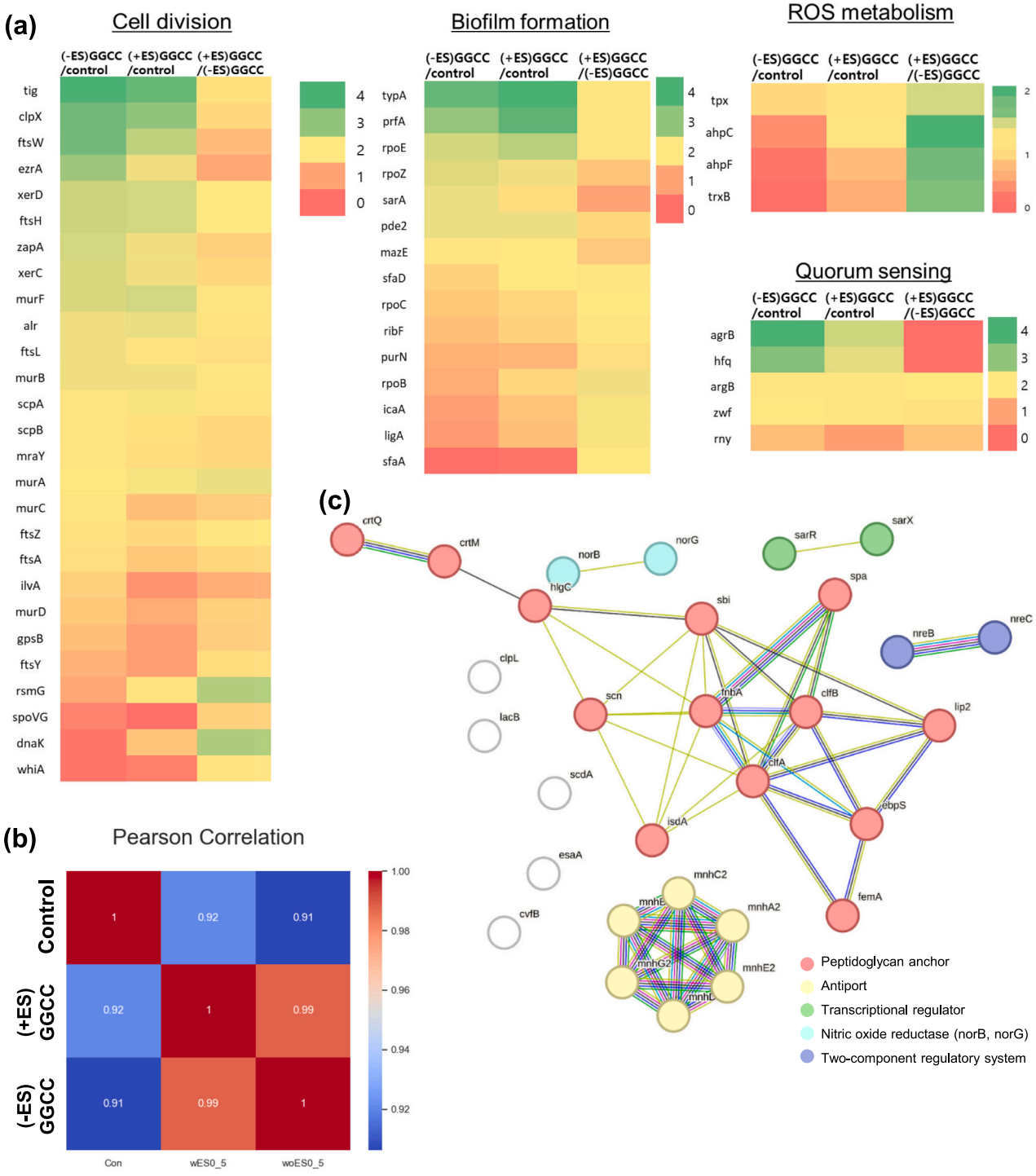

Fig. 10. Transcriptomic analysis of MRSA after treatment of stimulation and hydrogel (a) heatmaps of genes in cell division, biofilm formation, ROS metabolism, and quorum sensing, (b) Pearson correlation of control, -ES GGCC0.5 and + ES GGCC0.5, (c) STRING analysis of possible interacting genes.

transcription of stress- and biofilm-related genes [40]. The loss of either *rpoE*, or *rpoZ* leads to the dysregulation of biofilm synthesis and reduced tolerance to stress [41]. The *sarA* is a master regulator that promotes the biofilm development. It promotes the biofilm formation by activating the ica operon and repressing the proteases that degrade the biofilm architecture [42]. The *mazE* is a key regulator of the stress-response system, specifically the toxin-antitoxin (mazEF) system. The *mazE* plays a central role in the maintenance of biofilm in harsh environments. The loss of *mazE* suggests a reduced capacity to hold live bacterial cells within the biofilm matrix [43,44]. The reduced expression of genes, including *rpoZ*, *sarA*, *pde2*, and *mazE*, from the transcriptomic analysis revealed a multifaceted mechanism by which ES disrupts the biofilm stability and promotes bacteria clearance by synchronized down-regulation of stress and transcription regulators, indicating an extensive breakdown of MRSA's biofilm-generation capacity.

The ES is known to affect various cellular processes and also induces ROS generation. Upon evaluation of the transcriptomic data, we observed an upregulation of oxidative response genes in MRSA,

including *tpx*, *ahpC*, *ahpF*, and *trxB,* in the treatment group treated with ES compared to the group without ES. These genes are key components of the antioxidant defense mechanism of bacteria, which guards against the harmful effects of ROS. The elevated expression of these genes indicates that the bacterial cell is subjected to oxidative stress by ES, potentially as a result of redox imbalance in the bacterial membrane or disruption of the electron transport chain [45]. The *Tpx*, *AhpC* and *AhpF* collaborate to minimize the hyperoxides to prevent the oxidative damage [46]. An essential part of the thioredoxin system, *trxB* promotes the function of peroxidases such as *AnpC*, preserving the redox condition of important cellular enzymes [47]. All of these genes are upregulated, which is clear evidence that MRSA is experiencing excessive oxidative stress and using a redox buffering mechanism to survive [48].

Additionally, the transcriptomic data was analyzed to study the genes involved in quorum sensing. The genes, including *agrB* and *hfq*, were found to be significantly downregulated, while *zwf*, *rny*, and *argB* showed a slight reduction in expression. The downregulation of *agrB* and *hfq* indicates impaired quorum-sensing. The management of *Staphylococcus aureus* pathogenicity and the spread of biofilms depend heavily on the agr quorum sensing system, specifically the agrBDCA operon [49,50]. The autoinducing peptide (AIP), which triggers the AgrC-AgrA signaling cascade to regulate toxin synthesis, adhesion, and biofilm behavior, is processed and exported by *AgrB* specifically. *AgrB* downregulation indicates a disruption in autoinducer signaling, which would decrease coordinated group behaviors, such as production of virulence factors and the formation of biofilms [51]. Collectively, the downregulation of *hfq* and *agrB*, and the broader suppression of supporting metabolic and regulatory genes, imply that ES disrupts MRSA's quorum sensing, making it more difficult for the bacteria to coordinate biofilm formation, toxin release, and immune evasion. This likely contributes to the decreased virulence and biofilm destabilization observed during ES.

To sum up, our comprehensive transcriptomic study shows that MRSA responds to electrical stimulation via a conductive hydrogel in multiple ways. The pathways affected by ES GGCC0.5 are shown in Scheme 2. This is characterized by the coordinated downregulation of genes essential for cell division (*ftsW*, *ftsA*, *mraY*, *murC*), biofilm regulation (*sarA*, *pde2*, *mazE*), and quorum sensing (*agrB*, *hfq*), suggesting impaired cellular proliferation, structural cohesion, and virulence signaling. At the same time, the upregulation of oxidative stress-related genes (*tpx*, *ahpC*, *ahpF*, *trxB*) indicates that ES triggers intracellular ROS accumulation, placing the bacterial cells under redox stress. This is further compounded by the suppression of global transcriptional stabilizers (*rpoE*, *rpoZ*), pointing to disrupted gene expression control under environmental stress. These results collectively imply that the ES disrupts MRSA physiology at the systemic level, thereby limiting its capacity to proliferate, adapt, and form robust biofilms, ultimately leading to the observed antimicrobial effect. This transcriptomic finding offers important mechanistic insight into the use of ES as a non-antibiotic treatment for antibiotic-resistant bacterial illnesses. The STRING-based protein–protein interaction (PPI) network (Fig. 10c) highlights highly interconnected clusters of DEGs involved in peptidoglycan biosynthesis, transcriptional regulation, nitric oxide reductase, and two-component regulatory systems. These functional nodes suggest a coordinated bacterial stress response involving cell wall damage sensing, membrane

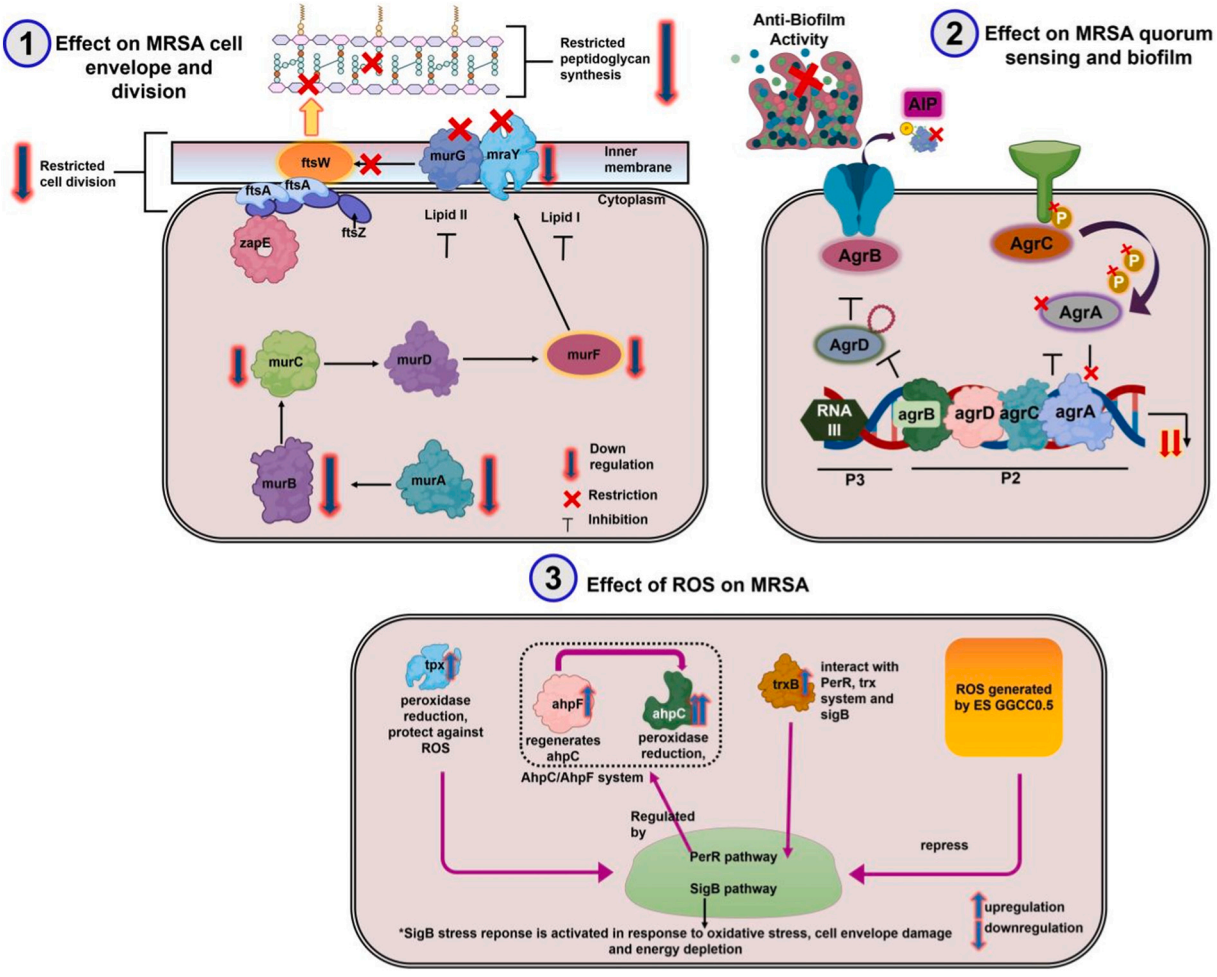

Scheme 2. Effect of (+)ES GGCC0.5 and changes in the pathway regulation based on the transcriptomic analysis: (1) effect on peptidoglycan layer synthesis, cell membrane synthesis, and cell division; (2) effect on quorum sensing and biofilm activity, and (3) effect of generation of ROS.

transport, and redox balance, all of which are critically disrupted by the GGCC hydrogel + ES condition.

To evaluate the overall similarity and reproducibility of gene expression profiles across different treatment groups, a Pearson correlation heatmap was constructed (Fig. 10b). The correlation coefficients ranged from 0.91 to 1.00, indicating high-quality and consistent transcriptomic data. The control group showed lower correlation with the hydrogel-treated groups (0.91 with −ES and 0.92 with +ES), suggesting substantial shifts in gene expression induced by the hydrogel. In contrast, a very strong correlation (0.99) was observed between the +ES GGCC0.5 and − ES GGCC0.5 hydrogel groups, reflecting their shared core transcriptomic response to the hydrogel material. However, despite the high correlation, further DEG and PCA analyses confirmed that electrical stimulation introduces distinct expression patterns on top of the hydrogel's baseline effect. Overall, the correlation analysis validates the robustness of the RNA-seq data and supports the conclusion that the hydrogel, with or without electrical stimulation, modulates the MRSA transcriptome.

3.9. Biocompatibility and biosafety of GGCC hydrogel

To assess the biocompatibility and regenerative potential of the hydrogels, we evaluated their effects on HDFs and keratinocytes using cell viability assays, live/dead staining, and qRT-PCR analysis of key wound-healing and keratinocyte-differentiation markers (Fig. 11). Both HDF and HaCaT cells exhibited high viability after 24 h exposure to all hydrogel formulations, including Gel, GGC, and GGCC0.5, with no significant cytotoxicity observed compared to the untreated control (Fig. 11a). Among the formulations, GGCC0.5 showed slightly enhanced viability in both cell types, suggesting that the incorporation of conductive uCNTs and chitosan does not compromise cellular compatibility but even supports cell proliferation. Cytotoxicity of hydrogels in the presence of NIR and ES was also evaluated for 24 h and 48 h, as shown in Figs. S5 and S6. The stimulation parameters showed no toxicity in HaCaT cells compared with the control groups. The scratch assay (Fig. S7) for in vitro wound-healing also showed that electrical stimulation did not have any adverse effects on HaCaT cells. These results indicate excellent cytocompatibility of the hydrogels, meeting the essential prerequisites for wound-dressing applications. Live/dead fluorescence imaging substantiated the viability assay results, revealing a predominance of live (green-stained) cells and very few dead (red-stained) cells across all conditions (Fig. 11b). White arrows indicate dead cells for clear detection. Both HDF and HaCaT cells demonstrated spreading, particularly in the GGCC0.5 group, indicating that the hydrogel microenvironment supports cellular attachment and growth. Notably, cell density appeared highest in the GGCC0.5 group, underscoring its superior biointerface properties. To further evaluate the impact of hydrogel on wound healing and epidermal regeneration, we analyzed the expression of keratinocyte differentiation markers (KRT1, KRT5, KRT14) in HaCaT and key wound healing genes (VEGF, Collagen I, TGF-β1) in HDF cells (Fig. 11c). GGCC0.5 significantly upregulated KRT1, KRT5, and KRT14 expressions compared to G and control, indicating enhanced support for keratinocyte maturation and proliferation. Moreover, expression of VEGF, Collagen I, and TGF-β1 was markedly increased in the GGCC0.5-treated group, demonstrating its strong potential to stimulate angiogenesis, extracellular matrix remodeling, and epithelial regeneration. Taken together, these findings confirm that GGCC0.5 hydrogels are not only cytocompatible but also actively promote cellular functions critical for wound healing. The synergistic integration of gelatin, chitosan, and conductive unzipped CNTs appears to create a favorable microenvironment that supports skin cells, including fibroblast and keratinocyte responses. Importantly, this biomaterial advances beyond passive wound coverage, functioning as an active biointerface to guide tissue repair at the molecular and cellular levels. However, further animal testing is required prior to clinical applications.

4. Conclusion

This study presents a novel, dual-stimuli responsive hydrogel system built upon a conductive chitosan matrix, offering a synergistic platform for advanced antibacterial and antibiofilm applications. Chitosan, a well-known natural polysaccharide with inherent antibacterial properties, served as the base material; however, its limited conductivity and moderate efficacy against resistant strains, such as MRSA, necessitated further functionalization. By integrating uCNTs into chitosan, we engineered a CC with enhanced electroactivity, NIR responsiveness, and antibacterial performance. This modified chitosan enabled effective electrical stimulation and NIR responsiveness, which dramatically enhanced the hydrogel's ability to disrupt robust MRSA biofilms and planktonic bacteria. RNA sequencing analysis revealed upregulation of stress response and membrane-disruptive genes, elucidating the molecular mechanism underlying its superior antibacterial and biofilm-disruptive activity. This approach offers an on-demand, antibiotic-free therapeutic approach that helps reduce continuous selective pressure, thereby minimizing the risk of antimicrobial resistance. Beyond its antibacterial potential, the incorporation of gelatin and bioactive RGD motifs into the hydrogel matrix supported excellent biocompatibility and proliferation. Moreover, hydrogel with both stimulations showed no toxicity towards keratinocytes. Overall, our conductive chitosan-based GGCC hydrogel platform represents a multifunctional, polysaccharide-derived material with significant promise as a candidate for skin tissue regeneration, bridging antibacterial efficacy, tissue regeneration, and stimuli responsiveness in a biocompatible, scalable system.

Supplementary data to this article can be found online at https://doi.org/10.1016/j.ijbiomac.2025.149845.

CRediT authorship contribution statement

Tejal V. Patil: Writing – original draft, Visualization, Project administration, Methodology, Investigation, Formal analysis, Data curation, Conceptualization. **Aayushi Randhawa:** Writing – original draft, Visualization, Methodology, Investigation. **Hyeonseo Park:** Visualization, Methodology, Investigation. **Rumi Acharya:** Writing – review & editing, Methodology, Investigation. **Sayan Deb Dutta:** Investigation. **Ki-Taek Lim:** Writing – review & editing, Validation, Supervision, Resources, Funding acquisition, Data curation.

Consent for publication

Not applicable.

Ethics approval and consent to participate

Not applicable.

Funding

This study was supported by the Basic Science Research Program through the National Research Foundation of Korea funded by the Ministry of Education (RS-2025-16065692; RS-2018-NR031068). This work was supported by Innovative Human Resource Development for Local Intellectualization program through the Institute of Information & Communications Technology Planning & Evaluation (IITP) grant funded by the Korea government (RS-2023-00260267).

Declaration of competing interest

The authors declare that they have no known competing financial interests or personal relationships that could have appeared to influence the work reported in this paper.

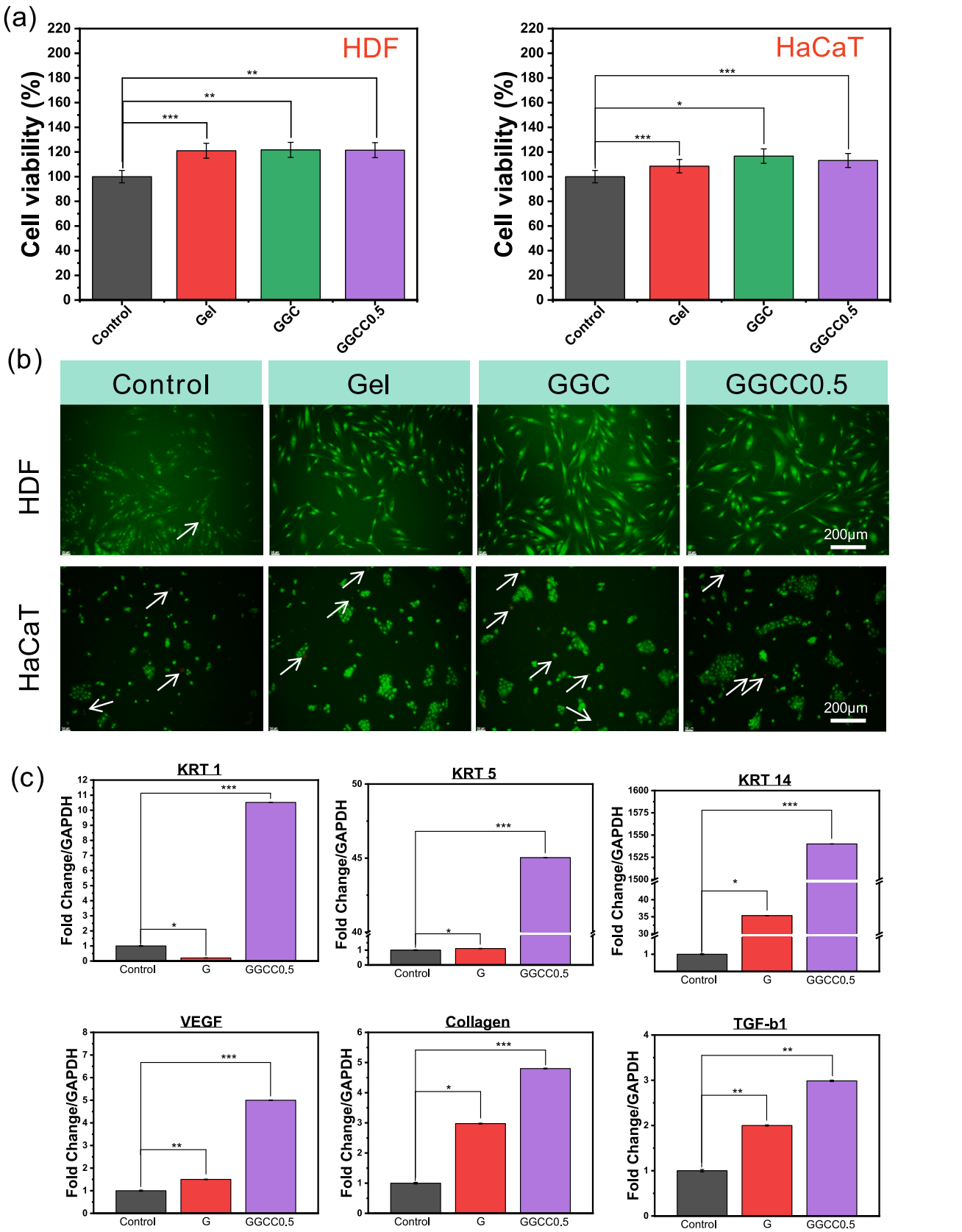

Fig. 11. Effect of hydrogels on fibroblasts (HDF) and keratinocytes (HaCaT), (a) biocompatibility, (b) live/dead assay (dead cells are indicated with white arrows), and (c) qRT-PCR for gene expression (number of replicates: $n = 4$, $^{*}p < 0.05$, $^{**}p < 0.01$, $^{***}p < 0.001$, and *n.s.*: not significant).

Data availability

All data generated or analyzed during this study are included in this article and its supplementary information files.

References

[1] F. Aflakian, F. Mirzavi, H.T. Aiyelabegan, A. Soleimani, J. Gholizadeh Navashenaq, I. Karimi-Sani, A. Rafati Zomorodi, R. Vakili-Ghartavol, Nanoparticles-based therapeutics for the management of bacterial infections: a special emphasis on FDA approved products and clinical trials, Eur. J. Pharm. Sci. 188 (2023) 106515.

[2] H. Khalili, S. Najar-Peerayeh, M. Mahrooghi, P. Mansouri, B. Bakhshi, Methicillin-resistant Staphylococcus aureus colonization of infectious and non-infectious skin and soft tissue lesions in patients in Tehran, BMC Microbiol. 21 (1) (2021) 282.

[3] K.W.K. Tang, B.C. Millar, J.E. Moore, Antimicrobial resistance (AMR), Br. J. Biomed. Sci. 80 (2023) 2023.

[4] A. Olumide Adekanmbi, R. Olamilekan Adesola, A. Olutoyin Adeyemi, C. C. Chinyere Mbionwu, The threat of methicillin resistant *Staphylococcus aureus* (MRSA) in the aquatic environment via wastewater generated from healthcare facilities, in: K. Garbacz, T.A. Jarzembowski (Eds.), Bacterial Infectious Diseases Annual vol. 2023, IntechOpen, Rijeka, 2023.

[5] N.A. Turner, B.K. Sharma-Kuinkel, S.A. Maskarinec, E.M. Eichenberger, P.P. Shah, M. Carugati, T.L. Holland, V.G. Fowler, Methicillin-resistant Staphylococcus aureus: an overview of basic and clinical research, Nat. Rev. Microbiol. 17 (4) (2019) 203–218.

[6] A. Zhao, J. Sun, Y. Liu, Understanding bacterial biofilms: from definition to treatment strategies, Front. Cell. Infect. Microbiol. 13 (2023) 2023.

[7] A.S. Chouhan, Overuse of antibiotics causes serious adverse effects in the body: a literature review, J Clin Med Health Care 1 (2) (2024) 1–4.

[8] X. Wang, M. Shan, S. Zhang, X. Chen, W. Liu, J. Chen, X. Liu, Stimuli-responsive antibacterial materials: molecular structures, design principles, and biomedical applications, Adv. Sci. 9 (13) (2022) 2104843.

[9] Y. Fu, M. Zhu, A. Shi, B. Zhang, P. Xu, Stimulus-responsive antibacterial strategies for construction of anti-infection bone implants, Next Materials 8 (2025) 100554.

[10] M. Ge, F. Jiang, H. Lin, Nanocatalytic medicine enabled next-generation therapeutics for bacterial infections, Mater. Today Bio 29 (2024) 101255.

[11] R. Yu, H. Zhang, B. Guo, Conductive biomaterials as bioactive wound dressing for wound healing and skin tissue engineering, Nano Micro Lett. 14 (1) (2021) 1.

[12] A. Harugade, A.P. Sherje, A. Pethe, Chitosan: a review on properties, biological activities and recent progress in biomedical applications, React. Funct. Polym. 191 (2023) 105634.

[13] Y. Zhou, Y. Zhang, Y. Nie, D. Sun, D. Wu, L. Ban, H. Zhang, S. Yang, J. Chen, H. Du, X. Pan, Recent advances and perspectives in functional chitosan-based composites for environmental remediation, energy, and biomedical applications, Prog. Mater. Sci. 152 (2025) 101460.

[14] J. Su, C. Liu, A. Sun, J. Yan, F. Sang, Y. Xin, Y. Zhao, S. Wang, Q. Dang, Hemostatic and antimicrobial properties of chitosan-based wound healing dressings: a review, Int. J. Biol. Macromol. 306 (2025) 141570.

[15] S. Lv, S. Zhang, J. Zuo, S. Liang, J. Yang, J. Wang, D. Wei, Progress in preparation and properties of chitosan-based hydrogels, Int. J. Biol. Macromol. 242 (2023) 124915.

[16] R. Kartik, S. Muthusamy, K. Shelly, M. Surendiran, Chemical modifications of chitin and chitosan fibers and filaments: a review, Macromol. Chem. Phys. 226 (12) (2025) 2400422.

[17] J. Tarique, S.M. Sapuan, N.F. Aqil, A. Farhan, J.I. Faiz, S. Shahrizan, A comprehensive review based on chitin and chitosan composites, in: S.S. M, I. Ahmad (Eds.), Composites from the Aquatic Environment, Springer Nature Singapore, Singapore, 2023, pp. 15–66.

[18] Y.Q. Almajidi, J. Gupta, F.S. Sheri, R.S. Zabibah, A. Faisal, A. Ruzibayev, M. Adil, M.J. Saadh, M.J. Jawad, F. Alsaikhan, A. Narmani, B. Farhood, Advances in chitosan-based hydrogels for pharmaceutical and biomedical applications: a comprehensive review, Int. J. Biol. Macromol. 253 (2023) 127278.

[19] C. Wang, Y.-S. Li, J. Jiang, W.-H. Chiang, Controllable tailoring graphene nanoribbons with tunable surface functionalities: an effective strategy toward high-performance Lithium-ion batteries, ACS Appl. Mater. Interfaces 7 (31) (2015) 17441–17449.

[20] M. Sabzevari, D.E. Cree, L.D. Wilson, Graphene Oxide–Chitosan Composite Material for Treatment of a Model Dye Effluent, ACS Omega 3 (10) (2018) 13045–13054.

[21] B.K. Głód, P. Piszcz, K. Czajka, P.K. Zarzycki, A new total antioxidant potential measurements using RP-HPLC assay with fluorescence detection, J. Chromatogr. Sci. 49 (5) (2011) 401–404.

[22] S.D. Dutta, K. Ganguly, A. Randhawa, T.V. Patil, D.K. Patel, K.T. Lim, Electrically stimulated 3D bioprinting of gelatin-polypyrrole hydrogel with dynamic semi-IPN network induces osteogenesis via collective signaling and immunopolarization, Biomaterials 294 (2023) 121999.

[23] T.V. Patil, S. Deb Dutta, D.K. Patel, K. Ganguly, K.-T. Lim, Electrospinning near infra-red light-responsive unzipped CNT/PDA nanofibrous membrane for enhanced antibacterial effect and rapid drug release, Appl. Surf. Sci. 612 (2023) 155949.

[24] C. Qiu, L. Jiang, Y. Gao, L. Sheng, Effects of oxygen-containing functional groups on carbon materials in supercapacitors: a review, Mater. Des. 230 (2023) 111952.

[25] D.G. Zarate-Triviño, E. Prokhorov, G. Luna-Bárcenas, J. Mendez-Nonell, J. B. González-Campos, E. Elizalde-Peña, J.D. Mota-Morales, P. Santiago-Jacinto, M. Terrones, S. Gómez-Salazar, S.M. Nuño-Donlucas, I.C. Sanchez, The effect of CNT functionalization on electrical and relaxation phenomena in MWCNT/chitosan composites, Mater. Chem. Phys. 155 (2015) 252–261.

[26] R. Varma, S. Vasudevan, Extraction, characterization, and antimicrobial activity of chitosan from horse mussel *Modiolus modiolus*, ACS Omega 5 (32) (2020) 20224–20230.

[27] W. Feng, Z. Wang, Tailoring the swelling-shrinkable behavior of hydrogels for biomedical applications, Adv. Sci. 10 (28) (2023) 2303326.

[28] S. Ahmed, F. Altaf, S.A. Khan, S. Manzoor, A. Ahmad, M. Mansha, S. Ali, R. Ata ur, K. Jacob, Probing the efficiency of PPMG-based composite electrolytes for applications of proton exchange membrane fuel cell, Trans. Tianjin Univ. 30 (3) (2024) 262–283.

[29] H. Holback, Y. Yeo, K. Park, 1 - hydrogel swelling behavior and its biomedical applications, in: S. Rimmer (Ed.), Biomedical Hydrogels, Woodhead Publishing, 2011, pp. 3–24.

[30] B. Söderström, K. Mirzadeh, S. Toddo, G. von Heijne, U. Skoglund, D.O. Daley, Coordinated disassembly of the divisome complex in Escherichia coli, Mol. Microbiol. 101 (3) (2016) 425–438.

[31] S. Schäper, A.D. Brito, B.M. Saraiva, G.R. Squyres, M.J. Holmes, E.C. Garner, Z. Hensel, R. Henriques, M.G. Pinho, Cell constriction requires processive septal peptidoglycan synthase movement independent of FtsZ treadmilling in Staphylococcus aureus, Nat. Microbiol. 9 (4) (2024) 1049–1063.

[32] D.P. Haeusser, R.L. Schwartz, A.M. Smith, M.E. Oates, P.A. Levin, EzrA prevents aberrant cell division by modulating assembly of the cytoskeletal protein FtsZ, Mol. Microbiol. 52 (3) (2004) 801–814.

[33] F.J. Gueiros-Filho, R. Losick, A widely conserved bacterial cell division protein that promotes assembly of the tubulin-like protein FtsZ, Genes Dev. 16 (19) (2002) 2544–2556.

[34] Y. Miao, Y. Chen, J. Luo, X. Liu, Q. Yang, X. Shi, Y. Wang, Black phosphorus nanosheets-enabled DNA hydrogel integrating 3D-printed scaffold for promoting vascularized bone regeneration, Bioact. Mater. 21 (2023) 97–109.

[35] S. Rausch, A. Hänchen, A. Denisiuk, M. Löhken, T. Schneider, R.D. Süssmuth, Feglymycin is an inhibitor of the enzymes MurA and MurC of the peptidoglycan biosynthesis pathway, ChemBioChem 12 (8) (2011) 1171–1173.

[36] S.L. Kuchma, J.P. Connolly, G.A. O'Toole, A three-component regulatory system regulates biofilm maturation and type III secretion in Pseudomonas aeruginosa, J. Bacteriol. 187 (4) (2005) 1441–1454.

[37] A. Neidig, A.T.Y. Yeung, T. Rosay, B. Tettmann, N. Strempel, M. Rueger, O. Lesouhaitier, J. Overhage, TypA is involved in virulence, antimicrobial resistance and biofilm formation in Pseudomonas aeruginosa, BMC Microbiol. 13 (1) (2013) 77.

[38] L. Pieta, F.B. Garcia, G.P. Riboldi, L.A. de Oliveira, A.P.G. Frazzon, J. Frazzon, Transcriptional analysis of genes related to biofilm formation, stress-response, and virulence in listeria monocytogenes strains grown at different temperatures, Ann. Microbiol. 64 (4) (2014) 1707–1714.

[39] X. Xue, J. Tomasch, H. Sztajer, I. Wagner-Döbler, The delta subunit of RNA polymerase, RpoE, is a global modulator of Streptococcus mutans environmental adaptation, J. Bacteriol. 192 (19) (2010) 5081–5092.

[40] A. Weiss, B.D. Moore, M.H.J. Tremblay, D. Chaput, A. Kremer, L.N. Shaw, The ω subunit governs RNA polymerase stability and transcriptional specificity in Staphylococcus aureus, J. Bacteriol. 199 (2) (2017).

[41] A. Weiss, D. Moore Brittney, H.J. Tremblay Miguel, D. Chaput, A. Kremer, N. Shaw Lindsey, The ω subunit governs RNA polymerase stability and transcriptional specificity in *Staphylococcus aureus*, J. Bacteriol. 199 (2) (2016), https://doi.org/10.1128/jb.00459-16.

[42] M.A. Tormo, M. Martí, J. Valle, A.C. Manna, A.L. Cheung, I. Lasa, J.R. Penadés, SarA is an essential positive regulator of Staphylococcus epidermidis biofilm development, J. Bacteriol. 187 (7) (2005) 2348–2356.

[43] A. Tripathi, P.C. Dewan, S. Ahmed, R. Varadarajan, MazF-induced growth inhibition and Persister generation in Escherichia coli*, J. Biol. Chem. 289 (7) (2014) 4191–4205.

[44] H. Valadbeigi, N. Sadeghifard, M.B. Salehi, Assessment of biofilm formation in Pseudomonas aeruginosa by antisense mazE-PNA, Microb. Pathog. 104 (2017) 28–31.

[45] C.L. Brinkman, S.M. Schmidt-Malan, M.J. Karau, K. Greenwood-Quaintance, D. J. Hassett, J.N. Mandrekar, R. Patel, Exposure of bacterial biofilms to electrical current leads to cell death mediated in part by reactive oxygen species, PLoS One 11 (12) (2016) e0168595.

[46] D. Parsonage, P.A. Karplus, L.B. Poole, Substrate specificity and redox potential of AhpC, a bacterial peroxiredoxin, Proc. Natl. Acad. Sci. 105 (24) (2008) 8209–8214.

[47] A. Ballal, A.C. Manna, Control of thioredoxin reductase gene (trxB) transcription by SarA in Staphylococcus aureus, J. Bacteriol. 192 (1) (2010) 336–345.

[48] A.J. Sporer, L.J. Kahl, A. Price-Whelan, L.E. Dietrich, Redox-based regulation of bacterial development and behavior, Annu. Rev. Biochem. 86 (1) (2017) 777–797.

[49] Y. Yamazaki, T. Ito, M. Tamai, S. Nakagawa, Y. Nakamura, The role of Staphylococcus aureus quorum sensing in cutaneous and systemic infections, Inflammation and Regeneration 44 (1) (2024) 9.

[50] S.Y. Queck, M. Jameson-Lee, A.E. Villaruz, T.H. Bach, B.A. Khan, D.E. Sturdevant, S.M. Ricklefs, M. Li, M. Otto, RNAIII-independent target gene control by the agr quorum-sensing system: insight into the evolution of virulence regulation in Staphylococcus aureus, Mol. Cell 32 (1) (2008) 150–158.

[51] S.T. Rutherford, B.L. Bassler, Bacterial quorum sensing: its role in virulence and possibilities for its control, Cold Spring Harb. Perspect. Med. 2 (11) (2012).